Radical chemistry at a rural site (Wangdu) in the North China Plain: Observation and model calculations of OH, HO$_2$ and RO$_2$ radicals

Zhaofeng Tan[1], Hendrik Fuchs[2], Keding Lu[1], Birger Bohn[2], Sebastian Broch[2], Huabin Dong[1], Sebastian Gomm[2,a], Rolf Häseler[2], Lingyan He[3], Andreas Hofzumahaus[2], Frank Holland[2], Xin Li[2], Ying Liu[1], Sihua Lu[1], Franz Rohrer[2], Min Shao[1], Baolin Wang[1], Ming Wang[4], Yusheng Wu[1], Limin Zeng[1], Yinsong Zhang[1], Andreas Wahner[2], and Yuanhang Zhang[1]

[1]College of Environmental Sciences and Engineering, Peking University, Beijing, China
[2]Institute of Energy and Climate Research, IEK-8: Troposphere, Forschungszentrum Jülich GmbH, Jülich, Germany
[3]Key Laboratory for Urban Habitat Environmental Science and Technology, School of Environment and Energy, Peking University Shenzhen Graduate School, Shenzhen, China
[4]School of Environmental Sciences and Engineering, Nanjing University of Information Science and Technology, Nanjing, China
[a]now at: d-fine GmbH, Opernplatz 2, 60313 Frankfurt, Germany

Correspondence to: K. Lu (k.lu@pku.edu.cn), H. Fuchs (h.fuchs@fz-juelich.de)

Abstract. A comprehensive field campaign was carried out in summer 2014 in Wangdu located in the North China Plain. A month of continuous OH, HO$_2$ and RO$_2$ measurements were achieved. Observations of radicals by laser induced fluorescence (LIF) technique gave daily maximum concentrations between $(5\text{-}15)\times10^6\,\text{cm}^{-3}$, $(3\text{-}14)\times10^8\,\text{cm}^{-3}$ and $(3\text{-}15)\times10^8\,\text{cm}^{-3}$ for OH, HO$_2$ and

5   RO$_2$, respectively. Measured OH reactivities (inverse OH lifetimes) were 10 to $20\,\text{s}^{-1}$ during daytime. A chemical box model constrained by trace-gas observations and based on a state-of-the-art chemical mechanism is used to interpret the observed radical concentrations. In general, the model can reasonably well reproduce measured radical concentrations during daytime. Like in previous field campaigns in China, modelled and measured OH concentrations agree for NO mixing ratios

10   higher than 1 ppbv, but systematic discrepancies are observed in the afternoon for NO mixing ratios of less than 300 pptv (the model-measurement ratio is between 1.4 to 2 in this case). If additional OH recycling equivalent to 100 pptv NO is assumed, the model is also capable of reproducing the observed OH concentrations for conditions of high VOC and low NO$_x$ concentrations with good agreement in HO$_2$ and RO$_2$. Observed RO$_2$ concentrations are underestimated in the morning

15   hours by a factor of 3 to 5. This indicates that an additional chemical source of RO$_2$ is missing in the model. The OH reactivity is also underpredicted in the early morning. Increasing VOC concentrations to match measured OH reactivity helps to reduce the discrepancy between modelled and measured RO$_2$. The underprediction of RO$_2$ coincides with high NO concentrations and therefore

leads to a significant underestimation of the local ozone production rates determined from the per-

20 oxy radical (HO_2 and RO_2) reactions with NO. The underestimation corresponds to a daily integral

ozone production of about 20 ppbv per day.

1 Introduction

Air pollution in Chinese megacity regions has become a problem of high concerns by citizens and the government. Ambitious restriction strategies were already implemented for the reduction
25 of the primary air pollutants sulfur dioxide (SO_2), nitrogen oxides (NO_x) and particular matter (PM_{10}) for more than a decade. Significant emission reductions of those primary air pollutants were achieved. However, high concentrations of secondary air pollutants, e.g. ozone (O_3) and small particles ($PM_{2.5}$) still occur and the air quality has even continuously been deteriorated at some places (Shao et al., 2006). As denoted in the Empirical Kinetics Modelling Approach (Ou et al., 2016), the
30 reduction in primary pollutants may not directly reduce O_3 due to the non-linearity of atmospheric photochemistry. Thus, a critical question is to find an optimized way to control the abundance of secondary air pollutants by the reduction of primary pollutants.

As shown in a large number of studies, hydroxyl radical (OH) chemistry controls the atmospheric oxidation globally (Stone et al., 2012; Ehhalt, 1999). However, also other oxidants can be of impor-
35 tance on a regional scale like NO_3 (Brown and Stutz., 2012), Criegee intermediates (Mauldin et al., 2012) and chlorine radicals (Thornton et al., 2010). In China, studies of atmospheric oxidants are still sparse (Lu et al., 2010; Wang et al., 2015). In summer 2006, we performed two field campaigns (PRIDE-PRD2006 and CareBeijing2006) focussing on hydroxyl and hydroperoxy (HO_2) radical measurements in a rural area in the Pearl River Delta (PRD) and in a suburban area (Yufa) close
40 to Beijing. The major results from these two campaigns were: 1) There were high concentrations of daytime and nighttime HO_x (=OH+HO_2) radicals in the Chinese developed megacity regions indicating a strong atmospheric oxidation capacity. 2) The high daytime OH concentrations at high concentrations of volatile organic compounds (VOC) and low NO_x concentrations could only be explained by introducing an additional OH regeneration process in the model that converts peroxy
45 radicals to OH like NO does. An equivalent of 0.8 ppbv and 0.4 ppbv of NO was required in PRD and Beijing, respectively. 3) The high daytime OH concentrations at high VOC and high NO_x conditions could be understood by model calculations (Hofzumahaus et al., 2009; Lu et al., 2012, 2013, 2014). A retrospective analysis (Rohrer et al., 2014) shows that the magnitude of unexplained OH concentrations observed in these two studies in China is similar to other OH observations at high
50 VOC conditions (Tan et al., 2001; Lelieveld et al., 2008; Whalley et al., 2011).

Because isoprene was the most important OH reactant during many of these campaigns, theoretical and laboratory investigations were done to investigate its photochemical degradation. Isomerization and decomposition reactions of organic peroxy radicals formed from isoprene were found to be competitive with the reaction of peroxy radicals with NO for conditions of these campaigns
55 (Peeters et al., 2009; Crounse et al., 2011; Fuchs et al., 2013; Peeters et al., 2014). They lead to the direct reformation of radicals and the production of hydroperoxy aldehydes (HPALD), which can photolyze and produce additional radicals. Isoprene chemistry was less important in our two field campaigns in China 2006 compared to other campaigns that were conducted in forested areas, so

that new findings in the degradation of isoprene alone could not close the gap between measured and
60   modelled OH (Lu et al., 2012, 2013).

As a continued effort to explore the hydroxyl radical chemistry in Chinese megacity areas, OH, HO_2, RO_2 radical concentrations and OH reactivity were measured for one month at a rural site (Wangdu) in the North China Plain in summer 2014 as part of a comprehensive field campaign. Several improvements have been achieved in comparison to the previous campaigns PRIDE-PRD2006 and CareBeijing2006. (1) Interference tests were performed for OH measurements applying a new prototype chemical-modulation device. (2) Unlike before, HO_2 was measured without interferences by RO_2 species that are formed from alkenes and aromatic VOCs. (3) Total RO_2 was measured together with OH and HO_2 in contrast to the two previous campaigns. (4) In addition, the sum of RO_2 species that are formed from alkenes and aromatic VOCs was measured as a separate class of RO_2. (5) Oxygenated VOCs (e.g., formaledehyde, acetaldehyde, isoprene oxidation products) were measured, whereas such observations were missing in the previous two campaigns. All improvements provide better constraints for the interpretation of the radical chemistry. The radical measurements were obtained by a newly built, compact instrument that combines resources from Peking University and Forschungszentrum Jülich. In this paper, we report results of radical measurements and model calculations in the context of previous campaigns investigating HO_x chemistry in China.

2   Methodology

2.1   Measurement site

The campaign took place between 7 June and 8 July 2014. The measurement site is close to the town Wangdu, which is a small city (population 260000 inhabitants) without major industry. The Taihang Mountains are located 50 km northwest of Wangdu and the Bohai sea 200 km east. The next large city, Baoding, is 35 km northeast of Wangdu. Beijing and Shijiangzhuang, two of the largest cities in the North China Plain, are located 170 km northeast and 90 km southwest of the site, respectively. Times given in this paper are CNST (Chinese national standard time = UTC + 8 h).

Instruments were set-up in a botanic garden, which was surrounded by farmland. Weeds and willows were the dominant tree species few of which were growing within 10 m to the instruments. There was no traffic by cars or trucks in the botanic garden; a nearby road was 2 km away. Most of the instruments were placed in seven sea containers. Two of them were stacked on top of three others and two more containers were placed approximately 5 m away from the other containers.

2.2   Instrumentation

90   A large number of trace gases and aerosol properties were measured during this campaign. Most of the instrument inlets were placed 7 m above the ground at the height of the upper containers. Table 1 summarizes the details of the trace gas measurements. OH, HO_2, and RO_2 radicals were

measured by laser induced fluorescence described in detail below. The OH reactivity (k_{OH}), which is the inverse chemical lifetime of OH was directly measured by a laser pump and probe technique

95 (Lou et al., 2010).

Most of the inorganic trace gases (O_3, CO, CO_2, NO, and NO_2) were simultaneously monitored by different instruments. O_3, CO and CO_2 measurements agreed well within their accuracies. O_3 measurements were performed by two commercial instruments using ultraviolet (UV) absorption (Environment S.A. model 41M, and Thermo Electron model 49i). Also SO_2, CO, CO_2 concentra-

100 tions were measured by commercial instruments (Thermo Electron model 43i-TLE, 48i-TLE and 410i). In addition, a cavity ring-down instrument (Picarro model G2401) provided measurements of CO, CO_2, CH_4 and H_2O concentrations.

Chemiluminescence technique was used to detect NO and also NO_2 after conversion to NO. Two commercial instruments were deployed by Peking University (PKU) (Thermo Electron model

105 42i NO-NO_2-NO_x analyzer), one of which (PKU-PL) was equipped with a home-built photolytic converter for the detection of NO_2 and the other with a catalytic converter (PKU-Mo). Another instrument was run by Forschungszentrum Jülich (FZJ) (Eco Physics model TR 780). Instruments were located in the upper two containers to make inlet lengths as short as possible in order to minimize the correction for shifts in the NO to NO_2 ratio by the reaction of NO with O_3 in the inlet

110 lines. The distance between inlets was less than 5 m. Measurements of the two PKU instruments and the FZJ instrument differed overall by ± 20 %, which cannot be explained by their calibration errors. The reason for this discrepancy is not clear. Calibrations of the FZJ instrument were less reproducible (10 %) as it used to be, while calibration measurements of the PKU instrument varied only by 1 to 2 %. Fortunately, the calibrations did not show a trend over time indicating that there

115 was no accumulation of contaminations in the inlet lines. Because of the better reproducibility of calibration measurements, NO and NO_2 measurements from PKU-Mo and PKU-PL instruments are used as model constraints in this study. However, the difference between measurements of different instruments is considered in the following as as additional uncertainty in the NO_2 and NO measurements.

120 Six instruments detected HONO using different techniques. Home-built instruments from FZJ (Li et al., 2014) and from PKU (Liu et al., 2016) utilized long-path absorption photometry (LOPAP). In addition, three instruments applied cavity enhanced absorption spectroscopy (CEAS) for the detection of HONO. They were operated by the US National Oceanic and Atmospheric Administration (NOAA) (Min et al., 2015), by the Anhui Institute of Optics and Fine Mechanics (AIOFM), and by

125 the University of Shanghai for Science and Technology (USST). A gas and aerosol collector (GAC), which is based on the wet denuder/ion chromatography technique, could also detect HONO (Dong et al., 2012). The agreement between measurements of all instruments was generally reasonable and comparison details will be presented in a future publication. HONO measurements from the FZJ-LOPAP instrument are used as model constraint for the following reasons: 1) the sensitivity of

130   instruments using cavity based absorption techniques are generally lower and some of the instruments had instrumental problems due to the degradation of the high reflectivity of the mirrors in the presence of high loads of aerosol during this campaign. 2) The GAC instrument can only be operated at a 30 min time resolution and the detection limit is only 300 pptv. 3) The FZJ-LOPAP instrument has been successfully deployed in various field campaigns. Nevertheless, differences between the

135   two LOPAP instruments of 20 % cannot be explained by the combined uncertainties and need to be considered as additional uncertainty of the HONO concnetrations (Liu et al., 2016).

59 organic species were measured by a gas chromatograph (GC) equipped with a mass spectrometer and a flame ionization detector (FID) (Wang et al., 2014). This instrument provided concentrations of C_2 to C_{11} alkanes, C_2 to C_6 alkenes, and C_6 to C_{10} aromatics. In addition, measurements

140   of volatile organic compounds (VOCs) were performed by a proton transfer reaction - mass spectroscopy system (PTR-MS, Ionicon). These measurements included isoprene, acetaldehyde, the sum of methyl vinyl ketone (MVK) and methacrolein (MACR), benzene, toluene, styrene, C_8-aromatics, C_9-aromatics, the sum of monoterpenes, and acetonitrile. Daytime measurements of the two instruments agreed well for those species which were detected by both instruments. During nighttime,

145   however, PTR-MS measurements gave much larger values compared to measurements by GC for some periods and some species. The reason for that is not clear, but could have been caused by interferences by other species that occur at the same mass in the PTR-MS. Because of this uncertainty mainly measurements by GC are taken as constraints for model calculation here. Only oxygenated species acetaldehyde, MVK and MACR that were only measured by PTR-MS are used. Formalde-

150   hyde (HCHO) was measured by a commercial instrument utilizing the Hantzsch method (Aerolaser GmbH model AL4021).

15 m south of the location of the containers, a 20 m high tower with meteorological instrumentation was set up, where temperature, pressure, relative humidity, wind speed and wind direction were measured at two different heights (10 and 20 m). The height of the planetary boundary layer (PBL)

155   could be estimated by a ceilometer (the minimum detectable PBL height was 200 m). Photolysis frequencies were calculated from the spectral actinic photon flux density measured by a spectroradiometer (Bohn et al., 2008), whose inlet dome was placed on top of the highest container.

More trace gases were detected, but will not be discussed in detail here: Peroxyacyl nitrates (PAN) and peroxypropionyl nitrate (PPN) were measured by gas chromatography with a electron-capture-

160   detector (Wang et al., 2010). H_2O_2 was collected by a scrubbing coil collector and detected by high-performance liquid chromatography (HPLC) coupled with post-column derivatization and fluorescence detection (Hua et al., 2008). Chemical ionization mass spectroscopy (CIMS) was utilized to measure nitryl chloride ($ClNO_2$) and N_2O_5, but measurements were only conducted after 21 June (Tham et al., 2016). A cavity enhanced absorption spectrometry instrument was deployed to detect

165   glyoxal, HONO and NO_2 (Min et al., 2015).

Aerosol properties were characterized in detail during the campaign, but will be discussed elsewhere. Measurements included particle number density and size distribution, and also chemical composition.

2.3 Laser-induced fluorescence instrumentation for the detection of radicals

170 #### 2.3.1 Instrument description

OH, HO_2 and RO_2 concentrations were measured by laser-induced fluorescence (LIF) technique. LIF is a direct method to detect OH radicals (Heard et al., 2003). In addition, HO_2 and RO_2 radicals can be detected by fluorescence after chemical conversion to OH (Fuchs et al., 2008).

The Peking University laser-induced fluorescence instrument, PKU-LIF, was deployed in this
175 campaign for the first time. It consists of two LIF measurement cells to detect both OH and HO_2. It was built by Forschungzentrum Jülich and is therefore similar to instruments described earlier (Holland et al., 1995; Hofzumahaus et al., 1996; Holland et al., 2003; Fuchs et al., 2011; Lu et al., 2012). Additionally, a third measurement cell was provided by Forschungzentrum Jülich for the detection of the sum of RO_2 radicals (Fuchs et al., 2008).

180 The instrument consists of a laser and a measurement module (Fig. 1). The laser radiation for the OH excitation at 308 nm is generated by a pulsed, frequency-doubled, tunable dye-laser system that is pumped by a commercial Nd:YAG laser (Spectra-Physics model Navigator) at 532 nm (repetition rate: 8.5 kHz; pulse duration 25 ns). The laser light is guided to the measurement cells, to the k_{OH} instrument, and to an OH reference cell by optical fibers. The laser power is divided with a ratio
185 of 0.6:0.32:0.08 resulting in a laser power inside the measurement cells of typically 20 mW. The signal of the reference cell, in which a large concentration of OH is produced by pyrolysis of water vapor on a hot filament, is used as a wavelength reference and allows for the automatic correction of possible drifts of the laser wavelength.

All components of the measurement module are housed in a weather-proof, air-conditioned box
190 placed on top of the upper container. For the OH and HO_2 detection cells, ambient air is sampled at a flow rate of 1 slpm (standard litre per minute, at standard conditions of 25 °C and 1atm) through conically shaped nozzles (Beam Dynamics, orifice diameter 0.4 mm) into low pressure cells ($p = 4$ hPa). RO_2 is measured by a differentially pumped system consisting of a chemical conversion reactor ($p = 25$ hPa), followed by a fluorescence detection cell ($p = 4$ hPa). 7 slpm ambient
195 air is sampled through a nozzle (orifice diameter 1.0 mm) into the reactor, half of which is sampled through a second orifice into the fluorescence cell. Nitrogen sheath flows of 1 slpm are surrounding the gas expansions of sampled air in all fluorescence cells. Reactive gases for the conversion of peroxy radicals can be injected via ring-shape nozzles in the fluorescence cells and via an injection needle in the RO_2 conversion reactor.

200   The laser light crosses the three fluorescence cells in a single pass. Microchannel plate photo-multiplier detectors (Photek, MCP 325) are used to detect photons collected by lens systems. The detection system is mounted perpendicular to the gas beam and laser light axis. The MCPs are gated to switch off the gain for the duration of the laser pulses. The OH fluorescence is recorded by a gated photon-counting system (Becker & Hickl, PMS 300) in a 500 ns time window starting approximately

205   100 ns after the laser pulse.

The total photon count-rate is composed of the OH fluorescence, solar stray light that enters the cell through the orifice, and laser stray light. The solar stray light is detected separately during a second counting window (duration of 25 µs starting 25 µs after the laser pulse), when the OH fluorescence signal has diminished. The long integration time ensures accurate subtraction of the

210   solar background signal, after it has been scaled to the shorter OH fluorescence counting window. The remaining other background signals are separated from the OH fluorescence by wavelength modulation of the laser. Background and fluorescence signals are measured together, when the laser wavelength is tuned on the OH absorption line, and only background signals are detected, when the laser wavelength is tuned away. A full wavelength cycle gives a time resolution of 32 s for one

215   radical measurement.

2.3.2 Interferences in the OH detection

It is known that O_3 photolysis by 308 nm radiation with subsequent reaction of O^1D with water vapor can produce artificial OH inside the measurement cell. This interference was characterized in laboratory experiments and parameterized taking laser power, O_3, and water vapor concentration

220   that were monitored. A correction is applied that is small compared to ambient OH concentrations: 50 ppbv of O_3 causes an equivalent of $3 \times 10^5 \, cm^{-3}$ OH for typical laser power (20 mW) and water concentration (1 %) in this campaign.

Potential interferences from ozonolysis reactions and NO_3 have been investigated for OH and HO_2 detection cells that are similar to the detection cells of the PKU-LIF instrument (Fuchs et al.,

225   2016). No significant interference was found from the ozonolysis of simple alkenes (e.g., ethene, propene), isoprene and monoterpenes at ozonolysis reaction rates of several ppbv h^{-1}, i.e. at reaction rates that are considerably higher than found in the atmosphere. Therefore, it is not expected that measurements in this campaign are affected by ozonolysis products. Interferences from NO_3 were reported (Fuchs et al., 2016). The underlying mechanism is still unknown. The magnitude of

230   the interference is $1.1 \times 10^5 \, cm^{-3}$ OH in the presence of 10 pptv NO_3. No significant interference is expected at NO_3 concentrations that are predicted by model calculations for the present campaign at nighttime (average 10 pptv).

Wavelength modulation used in this work to distinguish between OH fluorescence and background signals is not capable of discriminating ambient OH signals from signals caused by artifi-

235   cially produced OH in the detection cells. Because interferences from unknown, internal processes

have been reported for two other LIF instruments (Mao et al., 2012; Novelli et al., 2014), we have tested a chemical modulation scheme that was proposed and used by these authors. For this purpose, ambient OH is removed by an OH scavenger (propane) that is added to the sampled ambient air just before entering the fluorescence cell, so that any remaining OH signal could be attributed to inter-

240   nally produced OH. The propane concentration has to be chosen such that most of the ambient OH is removed while it is small enough to prevent OH losses inside the fluorescence cell. When the scavenger is replaced by nitrogen, the sum of ambient OH and possible interference OH is measured. By switching between propane and nitrogen addition, ambient OH signals can be discriminated from artifacts.

245   In the campaign, we applied a prototype device for chemical modulation which was temporarily attached to the OH detection cell for a few times. The device consisted of a Teflon tube with an inner diameter of $1.0\,\text{cm}$ and a length of $10\,\text{cm}$. About $20\,\text{slpm}$ of ambient air were drawn through the tube by a blower. $1\,\text{slpm}$ of air was sampled into the OH detection cell. At the entrance of the Teflon tube, either propane mixed with a flow of nitrogen or only nitrogen was injected into the air flow by a small

250   tube (stainless steel, outer diameter 1/16"). Due to technical problems with the control electronics, the device failed to operate in the first half of the campaign. In the second part of the campaign, it showed still instabilities causing an increased uncertainty in the determination of the OH scavenging efficiency. The two signals with and without propane have contributions from ambient OH (S_{OH}), from the known ozone interference (S_{O3}) and any potential additional interference signal (S_{int}):

255
$$S_{\text{N2}} = S_{\text{OH}} + S_{\text{O3}} + S_{\text{int}} \tag{1}$$
$$S_{\text{prop}} = (1 - \epsilon)S_{\text{OH}} + S_{\text{O3}} + S_{\text{int}} \tag{2}$$

ϵ is the titration efficiency, with which ambient OH is removed, when propane is added.

As long as ambient OH does not change while switching between the two measurement modes, the difference between the two signals can be used to calculate the signal from ambient OH:

260
$$S_{\text{OH}} = \epsilon^{-1}(S_{\text{N2}} - S_{\text{prop}}) \tag{3}$$

Together with the known ozone interference the signal that is expected to be observed in the absence of an additional interference can be calculated and compared to the total signal that is measured, if no OH scavenger is added (S_{N2}).

The accurate knowledge of the titration efficiency ϵ is essential for an accurate quantification of

265   potential interferences. The titration efficiency was determined before each ambient titration test using a radical source (see below). The value ranged between $80\,\%$ and $97\,\%$ depending on the amount of propane. The titration efficiency depended on both, the flow rate of propane and the flow rate of the additional nitrogen flow. 0.02 to $0.2\,\text{Liter/min}$ of a $5\,\%$ propane mixture in nitrogen and an additional flow of pure nitrogen with a flow rate between 0.04 and $0.5\,\text{Liter/min}$ were used. The

270   dependence of the titration efficiency on the flow rate shows that mixing of the injected flow into

the high flow of ambient air was inhomogeneous similar to results reported in (Novelli et al., 2014). Because of technical problems, the accuracy of ϵ is only 10 % at a fixed nominal propane flow.

The propane concentrations used in the chemical-modulation tests are not expected to influence possible OH interference signals, because the OH lifetime with respect to the reaction with propane is much longer than the residence time (3 ms) in the low-pressure detection cell.

Another systematic error could arise from depletion of ambient OH by wall loss in the attached Teflon tube. Calibrations of OH sensitivities with and without the titration unit only differed by 5 %, which indicates that wall loss was not important.

2.3.3 Interferences in the HO_2 measurement

The detection of HO_2 is achieved by chemical conversion to OH in its reaction with NO (Hard et al., 1995). Three types of interferences are known for the current instrument design.

A small OH signal is observed, when NO is injected into the fluorescence cell in the absence of ambient radicals. This background signal was regularly determined during each calibration and was stable over the entire campaign. The equivalent HO_2 concentration of this signal is $3 \times 10^7 \, \mathrm{cm}^{-3}$ for the NO mixing ratios applied in this campaign (see below). On the other hand, the ambient NO_3 radicals can also introduce interferences in HO_2 detection similar to OH cell (see above). The estimated interference is $1 \times 10^7 \, \mathrm{cm}^{-3}$ at 10 pptv of NO_3 (Fuchs et al., 2016), which is within the range of the detection limit.

Specific RO_2 radicals have the potential to be converted to OH on the same time scale as HO_2 (Fuchs et al., 2011), if the NO concentration is high enough. In the following, this class of peroxy radicals is denoted $RO_2^{\#}$. In previous papers (e.g. Lu et al., 2012), HO_2^* was defined as the sum of HO_2 and interferences from $RO_2^{\#}$ that are detected with the conversion efficiency $\alpha_{RO_2}^i$.

$$[HO_2{}^*] = [HO_2] + \sum \left(\alpha_{RO_2}^i [RO_2]_i \right) = [HO_2] + \alpha_{RO_2}^{\#} [RO_2^{\#}] \tag{4}$$

$RO_2^{\#}$ is then the sum of interfering RO_2 species that is converted with an averaged conversion efficiency $\alpha_{RO_2}^{\#}$.

A low NO concentration can minimize the potential impact of RO_2 conversion, because RO_2 conversion to OH requires one more reaction step with NO. Therefore, the NO concentration used for the conversion of HO_2 during this campaign was chosen to be significantly smaller than in previous field campaigns (Lu et al., 2012, 2013). Furthermore, the amount of NO was periodically switched between two concentrations, in order to test, if HO_2 measurements may have still been affected by interferences from $RO_2^{\#}$. In the beginning of the campaign, NO mixing ratios varied between 5 ppmv and 20 ppmv, yielding HO_2 conversion efficiencies of 11 % and 35 %, respectively. After 14 June, the mixing ratios were switched between values of 2.5 ppmv and 5 ppmv, giving lower HO_2 conversion efficiencies of 6 % and 11 %, respectively. During operation with alternating NO concentrations, the application of the higher NO concentration always yielded higher HO_2^* concen-

trations, as expected from the influence of $RO_2^{\#}$. The ratios of HO_2^{*} measurements obtained for a pair of alternating NO concentrations showed no temporal trend or diurnal variation. On the assumption that the contribution from $RO_2^{\#}$ scales linearly with the added NO concentration, correction factors for the determination of interference-free HO_2 concentrations were derived. The factors are 1.02,

310   1.05, and 1.2 for the addition of 2.5, 5, and 20 ppmv NO, respectively. The correction was then applied to generate a homogenous data set for HO_2.

2.3.4   Detection of RO_2

In the RO_2 detection system, the chemical conversion of RO_2 and of HO_2 to OH is accomplished by a two step process as described in Fuchs et al. (2008). In the first chamber (conversion reactor), the

315   addition of 0.7 ppmv NO and 110 ppmv CO at a pressure of 25 hPa leads to the conversion of OH and RO_2 to HO_2. The amount of NO in the reactor is optimized for complete conversion of CH_3O_2 to HO_2. Similar conversion efficiencies apply to the majority of other atmospheric RO_2 species, including those resulting from OH reactions with simple alkanes, monoalkenes and isoprene (Fuchs et al., 2008). If these are the dominating RO_2 species, then all sampled RO_X (=$OH+HO_2+RO_2$)

320   radicals are present as HO_2 at the exit of the conversion reactor. In the second chamber (fluorescence cell at a pressure of 4 hPa), HO_2 is converted to OH by increasing the NO mixing ratio to 0.5 %. In contrast to the pure HO_2 detection described above, there is no need to keep the HO_2 conversion efficiency small to avoid simultaneous RO_2 conversion. Therefore, the NO concentration is much higher compared to the NO concentration in the HO_2 detection system. This measurement mode

325   gives the total RO_2 concentration, when the contributions of OH and HO_2 measured in the other two cells are subtracted.

The RO_X system can be operated in a second mode. CO is still added to the converter, but NO is switched off, so that RO_2 radicals are not converted to HO_2. In the fluorescence cell, however, $RO_2^{\#}$ species are converted to OH on the same time scale as HO_2 at the high NO concentration. As a

330   result, this operational mode measures HO_2^{*} (Eq. 4). Subtraction of the HO_2 concentration measured in the HO_2 cell then allows to estimate the concentration of $RO_2^{\#}$ radicals (Whalley et al., 2013). A conversion efficiency of $\alpha_{RO_2}^{\#} = 0.8 \pm 0.2$ is applied here to calculate $RO_2^{\#}$ concentrations (Lu et al., 2012; Fuchs et al., 2011). The error of this value adds to the uncertainty of $RO_2^{\#}$ concentrations.

Like for the HO_2 detection system, the presence of NO alone causes background signals of $5.0 \times$

335    $10^7 \, cm^{-3}$ and $3.5 \times 10^7 \, cm^{-3}$ in the operational modes with and without NO addition in the conversion reactor. In addition, NO_3 causes an interference signal, which is equivalent to $1 \times 10^7 \, cm^{-3}$ RO_2 per 10 pptv NO_3 (Fuchs et al., 2016).

2.3.5   Calibration and detection limits

The calibration of the LIF instrument is achieved by a radical source that provides equal concentra-

340   tions of OH and HO_2 radicals by water vapor photolysis at 185 nm described in detail in Holland

et al. (2003). The radical concentrations delivered by the source can be calculated from the measured water vapour concentration and the intensity of the photolysis lamp with a $1\,\sigma$ accuracy of $10\,\%$. The calibration procedure to determine the sensitivity in the different modes of the HO_x and RO_x channels is achieved by conversion of OH to HO_2 and CH_3O_2 (Fuchs et al., 2008).

345   During the campaign, calibrations were done approximately every third day. No trend with time for any of the sensitivities was observed. Thus, averaged sensitivities over the entire campaign were applied to calculate radical concentrations. The variability of the measured sensitivities is considered as an additional calibration uncertainty. The reproducibility ($1\,\sigma$ standard deviation) of the sensitivity for the OH cell was $5\,\%$, and for the HO_x cell 5 and $10\,\%$ for the high and low HO_2 conversion

350 efficiencies. The reproducibilities of the sensitivities of the RO_x system were $7\,\%$ for the detection mode without NO in the conversion reactor and $12\,\%$ for the mode with NO.

    The detection limit depends on the sensitivity, on the value of the background signal, and on the integration time (Holland et al., 1995). For nighttime conditions in the absence of sunlight, the detection limits for a signal-to-noise ratio of two and a measurement time of $30\,\mathrm{s}$ during this

355 campaign were $0.32 \times 10^6\,\mathrm{cm}^{-3}$, $0.10 \times 10^8\,\mathrm{cm}^{-3}$ and $0.11 \times 10^8\,\mathrm{cm}^{-3}$ for OH, HO_2 and RO_2, respectively. During daytime, the detection limits for OH and HO_2 are significantly higher, because higher background signals from solar radiation are present. For example, the detection limit for OH increased by a factor of 5 for typical solar background signals around noon. The detection limit of the RO_x system is not different during day- and nighttime, because no significant solar radiation can

360 enter the fluorescence cell through the conversion reactor.

2.4 Model calculations

Measured radical concentrations are compared with results from box model calculations. The model is based on the compact Regional Atmospheric Chemical Mechanism version 2 (RACM) described in Goliff et al. (2013). This mechanisms includes 17 stable inorganic species, 4 inorganic interme-

365 diates, 55 stable organic compounds and 43 intermediate organic compounds. Compounds that are not explicitly treated in the RACM are lumped into species with similar functional groups. The assignment of organic compounds that were measured during this campaign to species in the RACM is listed in Table 2.

    Some modifications were applied to the RACM. The isoprene mechanism was replaced by the

370 more detailed mechanism listed in Table 4. It is based on the Leuven Isoprene Mechanism (LIM) proposed by (Peeters et al., 2009). Here, we use the updated LIM for bulk RO_2 reactions described in Peeters et al. (2014). In addition, the chemistry of the first generation products of the isoprene oxidation, MVKand MACR, and isoprene hydroperoxides (ISHP) are revised. MACR has been shown to regenerate OH via RO_2 isomerization and decomposition (Crounse et al., 2012; Fuchs

375 et al., 2014). OH is also formed by the reaction of RO_2 from MVK with HO_2 with a significant yield (Praske et al., 2015). The products of the reaction of isoprene hydroperoxides formed in the

reaction of isoprene RO_2 with HO_2 have been revised by Paulot et al. (2009) showing that epoxides can be formed in an OH neutral reaction.

Model calculations are constrained to measured trace gases, including inorganic species (H_2O,
380   NO, NO_2, O_3, HONO, CO) and organic species (methane and non-methane organic compounds listed in Table 2). Because only the sum of methyl-vinyl-ketone (MVK) and methacrolein (MACR) were measured, a ratio of 0.6:0.4 (Galloway et al., 2011) was used to divide the sum measurement to individual species. In addition, physical parameters like photolysis frequencies, temperature and pressure are constrained to measured values.

385   For model calculations, the measured time series are synchronized to equidistant 5 min time intervals. This is done either by averaging or by linear interpolation, if the time resolution of the measurement is shorter or longer than 5 min. Measurements of the two instruments for ozone and CO are combined, in order to fill data gaps.

The total OH reactivity measured in this campaign can be well explained most of the time by
390   the measured trace gases listed in Table 2. Consequently, there were no other relevant OH reactants in the atmosphere which would otherwise have contributed significantly to the measured reactivity. For this reason, long-lived product species which were not measured are constrained to zero in the model in order to avoid unrealistic build-up of additional reactivity. This constraint is consistent with the assumption that most of the measured pollutants were emitted nearby and were not much
395   photochemically aged. Only aldehydes (ALD) are not set to zero, because they lead to the formation of reservoir species for organic peroxy radicals (peroxy acyl nitrates, PAN and PPN), which are kept as free parameters. In addition, HPALD that is formed in the new isoprene chemistry is not constrained to zero. In order to avoid unrealistic accumulation of these species, an artificial, constant loss is added, which limits their lifetime to 24 hours.

400   For comparison with experimental RO_2 data, calculated RO_2 concentrations shown here only include those RO_2 species that can be detected by the measurement system. The largest fraction of RO_2 that are not included in the calculated RO_2 are NO_3-alkene adducts (RACM name OLND), because their reaction with NO does not produce HO_2. The largest concentration of OLND is predicted in the early evening (approximately $1 \times 10^8 \, cm^{-3}$). In contrast, the majority of modelled RO_2
405   during daytime consists of species which are detected. In the model, the observable RO_2 species contribute with equal weight to the total RO_2, whereas laboratory calibrations of the RO_2 instrument have shown slightly different (less than $\pm 20\%$) detection sensitivities for the measured RO_2 species (Fuchs et al., 2008).

3 Results and Discussion

3.1 OH chemical modulation tests

Chemical modulation tests as described in Section 2.3.2 were conducted on 29 June (afternoon), 30 June (morning and afternoon), 2 July (afternoon) and 5 July (afternoon and evening). The OH signal measured when no scavenger is added (S_{N2}) contains contributions from ambient OH, the interference from ozone, and possibly unknown interferences (Eq. 1). Fig. 2 shows results from all tests performed during this campaign. S_{N2} is compared to the sum of the known ozone interference (S_{O3}) and the concentration of ambient OH (S_{OH}), which is calculated according to Eq. 3 from the measurements with (S_{prop}) and without (S_{N2}) scavenger. The error bars in Fig. 2 are calculated from the measurement precision of the fluorescence signals S_{N2} and S_{prop}. In addition, the sum of S_{OH} and S_{O3} could be affected by a systematic error, which is dominated by the 1σ uncertainty of the titration efficiency (10 %) needed to calculate S_{OH}. This systematic error would result in a change of 0.3 to 0.5×10^6 cm^{-3} in S_{OH} (Eq. 3).

The total signals S_{N2} (Fig. 2) are on average higher than the corresponding sums of S_{OH} and S_{O3}. Although the differences are similar to the combined statistical errors of the measurements, they appear to be systematic. Differences vary between 0.5×10^6 and 1×10^6 cm^{-3} (average: $(0.85 \pm 0.3) \times 10^6$ cm^{-3}), which is on the order of 10 % of the total OH signal during daytime, when no scavenger is applied. The differences are within the the 2σ systematic error of S_{OH}. Thus, the differences between S_{N2} and $S_{OH}+S_{O3}$ are at the limit of detection of the experimental setup used in the campaign. Quantitatively similar differences (up to 1×10^6 cm^{-3}) were obtained in the chemical modulation tests on other days.

The observed differences could be the result of a systematic error in the determination of S_{OH} or could be caused by an unknown OH interference. In case of an interference, it would be a small fraction of the total measured OH during daytime. The measured nighttime OH, however, would be much stronger affected. Because the existence of an unknown OH interference cannot be ruled out by the test results in this campaign, the interpretation of the radical chemistry will concentrate on daytime conditions. More precise and accurate chemical modulation tests with an improved experimental set-up are needed in future field campaigns.

3.2 Meteorological and chemical conditions

Meteorological conditions were characterized by high temperatures of up to 37 °C and high humidity. The wind velocity was usually below 2 m/s. Back trajectory analysis using the NOAA HYSPLIT (Hybrid Single Particle Lagrangian Integrated Trajectory Model) model (Stein et al., 2015) showed that air masses were usually transported from south or east where large city clusters are located. Solar radiation was strong during this campaign with few exceptions of hazy or cloudy days (15 to 19, 25 June and 1 to 4 July, Fig. 3).

Afternoon CO mixing ratios increased during several periods indicating accumulation of anthro-
pogenic emissions on a regional scale. They are separated by sudden drops during rain events on 19
June and 4 July and on 27 and 28 June when clean air was transported from the north.

During the first half of the campaign, burning of agricultural waste after harvesting on surrounding
fields was observed. This was confirmed by high acetonitrile mixing ratios (>1 ppbv) from 12 to
19 June. Biomass burning was accompanied by a reduced visibility and an increase in aerosol mass
concentrations ($PM_{2.5}$) with maximum values of $150 \, \mu g \, cm^{-3}$ on 16 June (campaign average value:
$70 \, \mu g \, cm^{-3}$).

Time series of O_3 and NO_2 showed often similar trends like CO, but were also strongly influ-
enced by photochemistry. Maximum daily ozone mixing ratios ranged between 100 and 140 ppbv
depending on the strength of radiation. Because solar radiation was attenuated between 14 and 19
June during the first pollution episode, O_3 peaked already on 14 June. O_3 was often completely
titrated by nitrogen monoxide during night.

Isoprene mixing ratios exhibited a typical diurnal profile with maximum values between a few
hundred pptv and nearly 4 ppbv in the afternoon. These values indicate that chemical conditions
were also influenced by presumably local biogenic emissions.

3.3 Time series of measurements and model calculations

The time series of measured and modelled OH, HO_2, RO_2 and k_{OH} are shown in Fig. 4. Distinct di-
urnal profiles are observed for all radical species. The daily maxima of OH, HO_2 and RO_2 appeared
around noontime and concentrations ranged between $(5-15) \times 10^6 \, cm^{-3}$, $(3-14) \times 10^8 \, cm^{-3}$ and $(3-15) \times 10^8 \, cm^{-3}$. On 18, 19 and 25 June and from 1 to 3 July, radical concentrations were small due
to attenuated solar radiation. On 28 June, OH raised to exceptionally high concentrations of up to
$3 \times 10^7 \, cm^{-3}$ for a short period of time, which was accompanied by an increase of the HONO mix-
ing ratio to 2 ppbv, so that OH production was enhanced by HONO photolysis. During this time,
farmland next to the measurement site was treated with water and artificial nitrogen-containing fer-
tilizer, which may have caused large, local HONO emissions.

In general, the model reproduces well the measured time series of OH, HO_2 and RO_2. Differences
between modelled and measured radical concentrations are generally smaller than the combined 1σ
uncertainties of radical measurements (10 %) and model calculations (40 %). The relatively large
uncertainty of the model calculations is a combination of uncertainties in the measurements used
as model constraints and reaction rate constants (for details see Lu et al. (2012)). Differences in
the measurements of NO and HONO from different instruments (20 % for both species) change
modelled OH concentrations by only 7 % and 5 %, if measurements from one or the other instrument
is taken as constraint.

A closer look at the modelled and measured radical concentrations reveals some systematic trends.
Modelled OH concentrations tend to be smaller than measurements during afternoon hours and

480 modelled RO_2 concentrations tend to be lower in the early morning and higher in the evening than corresponding RO_2 measurements. In contrast, differences between modelled and measured HO_2 concentrations are small at all times. Because of the similarity of the model-measurement agreement for different days, further analysis of daytime radical concentrations will be done on the basis of median diurnal profiles (Section 3.4).

485 The OH observed at night are mostly above the limit of detection ($3 \times 10^5 \, \mathrm{cm}^{-3}$) with concentrations around $5 \times 10^5 \, \mathrm{cm}^{-3}$, whereas the model predicts concentrations below the limit of detection. In a few nights, the measured OH is even higher (e.g., 1-3 $\times 10^6 \, \mathrm{cm}^{-3}$ on 13 June). The reason why the measured OH values are significantly above the model prediction is not clear. It could be caused by missing chemistry in the model or vertical gradients in the nocturnal boundary layer as discussed

490 in Lu et al. (2013). Furthermore, we cannot exclude an unknown interference of the same magnitude. The known interference from NO_3 is probably not sufficient as an explanation (Fuchs et al., 2016). Using NO_3 concentrations from the model (average. 10 pptv), the expected interference would be less than $1 \times 10^6 \, \mathrm{cm}^{-3}$ for this campaign. Thus, if interferences played a role, they would probably have a different origin.

495 The time series of measured OH reactivity shows a change on 20 June (Fig. 4). During the first two weeks, diurnal profiles of k_{OH} are more structured and show higher values with maximum values of up to $40 \, \mathrm{s}^{-1}$ compared to values after 20 June, when k_{OH} is only around $10 \, \mathrm{s}^{-1}$ in the afternoon and exhibits a less distinct diurnal profile. The first period coincides with the accumulation of pollutants like CO, nitrogen oxides and particles (Fig. 3). In addition, harvesting and biomass burning activities

500 caused local emissions of OH reactants, which may explain the short-term increases in OH reactivity during this period, especially during nighttime, when fresh emissions are released into the shallow nocturnal boundary layer and highest OH reactivity is observed. After 20 June, biomass activities close to the measurement place were less often observed and heavy rainfall cleaned the air.

 In the first period of the campaign, the model often underpredicts the measured OH reactivity,

505 especially at night. This is likely caused by unmeasured atmospheric compounds from local emission sources like biomass burning. In the second period, the modelled and measured reactivities agree well at day and night for most of the time.

3.4   Median diurnal profiles

 Differences between measurements and model calculations are further analyzed as median diurnal

510 profiles with a time resolution of one hour (Fig. 5). Only data is included, when measurements of all key species used as model constraints and radical measurements are available at the same time. Therefore, four days are excluded from the analysis from the entire data set. On 13 June, data gaps are larger than 6 hours for nearly all instruments. No measurements of VOCs are available on 14 June, no measurements of photolysis frequencies on 22 June and no radical measurements on 4

515 July. The number of data points in the median profiles from the first period of the campaign before

20 June is less than the number of data points from the period after 20 June. On the one hand the length of the first period is shorter and on the other hand there are more data gaps in the beginning of the campaign. Therefore, only one third of the data points included in the median diurnal profile originates from days before 20 June. Chemical conditions of data included in the median profile
520   are summarized in Table 3 and median diurnal profiles of important photochemical parameters are shown in Fig. 6.

Median measured OH concentrations are approximately $1 \times 10^6 \, \text{cm}^{-3}$ larger than model calculations in the afternoon. At the same time, the median NO mixing ratio drops from 0.3 to 0.1 ppbv (Fig. 6). Although newly proposed isoprene mechanisms have the potential to enhance the OH re-
525   generation for low NO_x condition, they only have a small effect on modelled OH concentration in this study due to the moderate NO (> 0.1 ppbv) and isoprene (typically less than 2 ppbv) concentrations. HO_2 concentrations are well reproduced by the model during daytime. The discrepancy between measured and modelled RO_2 is analyzed in detail in Section 3.7.

Measured k_{OH} is high during night, peaks in the morning ($22 \, \text{s}^{-1}$) and decreases to about $11 \, \text{s}^{-1}$
530   in the afternoon. Modelled k_{OH} shows a relative flat diurnal profile (average over the day is $14 \, \text{s}^{-1}$). Whereas good agreement with measurements is achieved during daytime, measured reactivity is higher during nighttime especially during the first part of the campaign. This is likely caused by unmeasured emitted OH reactants. A sensitivity model run, in which product species are not constrained to zero as in this model run, does not give significantly different OH reactivity in the night.
535   A more detailed analysis of the OH reactivity in this campaign will be published in a separate paper.

3.5   Correlation of OH with j(O^{1}D)

Strong correlation has been found between j(O^{1}D) and OH radical concentrations for many field campaigns in different environments from marine to continental locations (Ehhalt and Rohrer, 2000; Brauers et al., 2001; Berresheim et al., 2003; Rohrer and Berresheim, 2006; Lu et al., 2012, 2013).
540   A strong linear correlation is also observed for data from this campaign (Fig. 7). A linear fit between measured OH concentrations and measured photolysis frequencies yields a slope of $4.5 \times 10^{11} \, \text{s cm}^{-3}$. This value is similar to values that were derived in previous field campaigns in China in 2006 in the Pearl River Delta and Yufa (Lu et al., 2012, 2013).

The intercept of the linear fit for the campaign in Wangdu is $1.0 \times 10^6 \, \text{cm}^{-3}$, which is smaller than
545   intercepts obtained for the data set from the campaigns in the Pearl River Delta ($2.4 \times 10^6 \, \text{cm}^{-3}$, Lu et al. (2012)) and Yufa ($1.6 \times 10^6 \, \text{cm}^{-3}$, Lu et al. (2013)). The intercept gives an estimate of the importance of radical sources when the production of O^{1}D from ozone is small. This includes non-photolytic sources (e.g. ozonolysis of VOCs) and photolytic processes in the early morning before j(O^{1}D) starts to rise (Fig. 10).
550   Modelled OH also shows a strong dependence on j(O^{1}D) with a slightly smaller intercept compared to the fit result taking the measurements.

3.6 Model-measurement comparison of RO_2

Figure 8 shows the speciation of RO_2 radicals in the model. Measurements give only the total RO_2 concentration of species that are efficiently converted to HO_2 by the reaction with NO on either a very short time scale of milliseconds ($RO_2^{\#}$) or on a time scale of one second (RO_2) in the measurement system. The median diurnal profiles for both classes of measured RO_2 are similar, but $RO_2^{\#}$ dominates in the early morning hours until 09:00. Its relative contribution becomes less in the evening. This is also predicted by the model. In the morning, however, the concentrations of RO_2 and $RO_2^{\#}$ species predicted by the model are 1 to $2 \times 10^8\,cm^{-3}$ smaller than measurements. Good agreement is achieved for total RO_2 and $RO_2^{\#}$ in the late afternoon. In the first half of the night, modelled total RO_2 is larger than measured RO_2. This mainly concerns RO_2 species that are not detected as $RO_2^{\#}$.

The strong underprediction of the observed RO_2 by more than a factor of four in the morning cannot be explained by the measurement error of RO_2 (see Section 2.3.4 and 2.3.5) and points to a model deficiency. Differences between measured and modelled RO_2 in the morning are mainly related to higher measured $RO_2^{\#}$. This could be a hint that the model does not adequately describe RO_2 chemistry from alkenes or larger organic compounds, because $RO_2^{\#}$ species are formed from their chemical transformation.

Model sensitivity runs show that a primary RO_2 source of 2 to $4\,ppbv\,h^{-1}$ would be required, in order to fill the gap in RO_2 in the morning (06:00 to 12:00). In this case, however, OH concentrations would increase to values that are significantly higher than measurements due to the efficient conversion from RO_2 to OH at high NO concentrations at this time of the day. Therefore, an unknown primary RO_x source alone can be excluded as reason for elevated RO_2.

One possible candidate for an additional RO_2 source is the photolysis of nitryl chloride ($ClNO_2$). High concentrations of $ClNO_2$ were observed in Wangdu from 20 June to 8 July in the early morning. The concentrations reached maximum values of 0.5 ppbv and decayed after 08:00 (Tham et al., 2016). Nitryl chloride is formed from heterogeneous reactions of nitrogen pentoxide (N_2O_5) (Osthoff et al., 2008) during nighttime. Its photolysis is a source of chlorine atoms in the morning, which can abstract H-atoms from hydrocarbons and directly produce RO_2. A sensitivity model run including chlorine chemistry described in Xue et al. (2015) gives a maximum Cl production rate of 0.2 pptv/h at 08:00. In this model run, a $ClNO_2$ source is assumed that leads to a linear increase of $ClNO_2$ to a maximum value of 0.5 ppbv during nighttime and early morning until 08:00 on each day. After 08:00 the modelled source is turned off and all $ClNO_2$ is photolyzed (photolysis rates are calculated from the measured actinic flux). The fast reaction of Cl with VOCs produces additional RO_2. However, this additional RO_2 source is not large enough to resolve the discrepancy between measured and modelled RO_2. Even if the modelled source strength is increased to match highest $ClNO_2$ mixing ratios of 2 ppbv observed at 08:00 on 21 June, additional primary production of

RO_2 from Cl oxidation is only $0.5\,\mathrm{ppbv\,h^{-1}}$ on average, an order of magnitude less than required to explain observed RO_2 concentrations.

The largest relative difference between modelled and measured RO_2 is observed in the early morning between 06:00 and 09:00. This is accompanied by high measured OH reactivity which is not reproduced by the model. Therefore, also the production rate of RO_2 could be underestimated by the model. In a sensitivity model run, the gap in the OH reactivity is filled by scaling VOC concentrations to match measurements. In this case, the gap between measured and modelled RO_2 concentrations can be partly closed before 09:00 without affecting the good agreement of OH and HO_2 indicating that OH reactants that are oxidized in the early morning are missing in the model.

The overprediction of RO_2 by the model in the evening could be related to the differences in the chemistry of RO_2 during day and night. The inability of the model to predict RO_2 in the night could be partly caused by strong fluctuations around the limit of detection of the instrument of $60\,\mathrm{pptv}$ in the measured NO concentrations used as constraint. Assuming no RO_2 production from NO_3 chemistry would bring measured and modelled RO_2 into agreement.

3.7 NO dependence of the radical concentrations

NO_x plays a crucial role in RO_x chemistry due to radical propagation via peroxy radical reactions with NO and radical loss by the reaction of OH with NO_2 (Ehhalt, 1999). Because of these two counteracting processes, maximum OH concentrations are expected at NO_x mixing ratios of a few ppbv at otherwise constant conditions.

Figure 9 shows measured and model radical concentrations depending on the NO mixing ratio. In order to reduce the influence of the OH production strength by photolysis, OH concentrations are normalized to $j(O^1D)$ measurements. In addition, only daytime values at NO concentrations above the detection limit of the NO instrument are included in this analysis ($j(O^1D) > 0.5 \times 10^5\,\mathrm{s^{-1}}$, $NO > 60\,\mathrm{pptv}$). Measured OH concentrations appear to be nearly independent on the NO concentration after normalization to $j(O^1D)$. Median values of measurements are almost constant with $7 \times 10^6\,\mathrm{cm^{-3}}$ for NO mixing ratios of up to $5\,\mathrm{ppbv}$. This behavior is only expected for NO mixing ratios between 0.3 and $3\,\mathrm{ppbv}$ as indicated by the base model calculations. Median modelled OH concentrations are nearly half of the median measured values ($5 \times 10^6\,\mathrm{cm^{-3}}$) at NO mixing ratios below $100\,\mathrm{pptv}$. This discrepancy is also seen in the median diurnal profile of measured and modelled OH (Fig. 5), but it is less pronounced, because NO mixing ratios only dropped below $0.3\,\mathrm{ppbv}$ for certain times and not on every day.

A similar OH behavior as the one shown in Fig. 9 has been reported for PRD and Yufa (Lu et al., 2012, 2013) and also for other field campaigns selected for conditions with high OH reactivity ($> 10\,\mathrm{s^{-1}}$) (Rohrer et al., 2014). In contrast, campaigns in relatively clean air have shown a decreasing trend of OH at low NO concentrations as expected from the reduced radical recycling efficiency (Holland et al., 2003).

Measurements and model calculations show similar decreasing trends for both, HO_2 and RO_2,
with increasing NO concentrations. This is expected, because the lifetime of these radical species
are mainly limited by their reactions with NO. As also seen in the median diurnal profiles (Fig. 5),
modelled and measured HO_2 concentrations agree within 20 % over the entire range of NO con-
centrations, whereas the measured RO_2 decreases less than the modelled RO_2 when NO increases.
At 3 ppbv NO modelled RO_2 concentrations become less than $1 \times 10^8 \, cm^{-3}$, whereas the median
measured RO_2 concentration remains at $3.5 \times 10^8 \, cm^{-3}$. As a consequence, the measured peroxy
radicals yield higher calculated net ozone production rates than the model (see Section 3.8).

Two sensitivity model runs were done. In the first sensitivity run, the model did not include the
updated isoprene mechanism, which is part of the base model run. The overall impact of the new
isoprene chemistry is rather small, the maximum increase in the median OH and HO_2 concentrations
due to the additional OH recycling is less than $1 \times 10^6 \, cm^{-3}$ and $1 \times 10^8 \, cm^{-3}$, respectively, at NO
mixing ratios smaller than 0.1 ppbv. This is smaller than the variability of measurements.

In the second sensitivity run, radical recycling was enhanced by introducing an artificial species
X that behaves like NO, but does not produce ozone (Fig. 9). This has been successfully applied
to describe unexplained high OH concentration in other campaigns (Rohrer et al., 2014) including
our previous observations in China (Hofzumahaus et al., 2009; Lu et al., 2012, 2013). Similar to
the observations in the previous campaigns, a constant mixing ratio of X would bring modelled
and measured OH into agreement for the entire range of NO concentrations (Fig. 9). Here, the
concentration of X needs to be equivalent to 100 pptv NO. Modelled HO_2 and RO_2 concentrations
do not change much, if this mechanism is applied.

OH concentrations in this campaign are better predicted by the base model compared to our previ-
ous field campaigns that were conducted in China. In all three campaigns, median diurnal profiles of
measured and modelled OH agree in the morning, but measured median OH starts to be increasingly
higher than modelled OH after noontime. In this campaign, the difference is a factor of 1.4 at 16:00
and a factor of two at sunset (18:00). Differences are within the $2\,\sigma$ uncertainty of measurements
for most of the time. In contrast, the difference was a factor of 2.6 to 4.5 in previous campaigns
for higher OH reactivity conditions. Consequently, also the amount of additional recycling that is
required to bring modelled and measured OH into agreement is less in this campaign (100 pptv NO
equivalent) compared to Yufa (400 pptv) and PRD (800 pptv) in 2006. The major differences be-
tween this campaign and the othres are: (1) OH concentrations in this campaign are smaller. (2) NO
mixing ratios (100 pptv) were lower in previous campaigns, reducing the OH recycling efficiency
from the reaction of peroxy radicals with NO. (3) Measured OH reactivity is around $12 \, s^{-1}$ in this
campaign, but was at least 50 % larger in the other campaigns. This is also larger than the modelled
reactivity in this campaign.

3.8 Ozone production rate

660 Peroxy radical measurements allow to calculate net ozone production (Mihelcic et al., 2003). The photolysis of NO_2 produces O_3 and NO. Because O_3 can also be consumed in the back-reaction of NO to NO_2, net ozone production is only achieved, if the reformation of NO_2 does not involve O_3. This is the case, if peroxy radicals (HO_2 and RO_2) react with NO. Therefore, net ozone production can be calculated from the reaction rate of peroxy radicals with NO using measured and modelled

665 peroxy radical concentrations (Fig. 5). Production ($P(O_3)$) is reduced by the loss of NO_2 via its reaction with OH and further losses of ozone ($L(O_3)$), which includes the loss via photolysis and reactions with OH, HO_2 and alkenes:

$$
\begin{aligned}
P(O_3) &= k_{HO_2+NO}[HO_2][NO] + \sum(k^i_{RO_2+NO}[RO^i_2][NO]) \\
&\quad - k_{OH+NO_2}[OH][NO_2] - L(O_3)
\end{aligned} \tag{5}
$$

670
$$
\begin{aligned}
L(O_3) &= \left(\theta\, j(O^1D) + k_{OH+O_3}[OH] + k_{HO_2+O_3}[HO_2]\right)[O_3] \\
&\quad \left(+ \sum(k^i_{alkene+O_3}[alkene^i])\right)[O_3]
\end{aligned} \tag{6}
$$

θ is the fraction of O^1D from ozone photolysis that reacts with water vapor.

The calculation of the net ozone production from measurements is complicated by differences in the reaction rate constants of NO with different RO_2 species. An effective rate constant is used

675 for the reaction of the total RO_2 with NO. The effective rate constant is determined from the rate constants of the different RO_2 species in RACM and their relative abundance calculated by the model for each instant of time. The derived effective rate constant increases in the morning and reaches a maximum $8.5 \times 10^{-12}\,cm^3\,s^{-1}$ in the afternoon and decreases to a value of $6.5 \times 10^{-12}\,cm^3\,s^{-1}$ after dusk. For comparison, the rate constant for the reaction of CH_3O_2 with NO is $7.5 \times 10^{-12}\,cm^3\,s^{-1}$.

680 A systematic underestimation of the calculated ozone production rate may arise from RO_2 species, which react with NO and form NO_2 but no HO_2 as products. Such RO_2 species would possibly contribute to the ozone formation, but are not detected in our instrument. As explained in Section 2.4, this behavior is found in the Wangdu campaign for peroxy radicals which are formed by reactions of alkenes with NO_3. However, because NO_3 is easily photolyzed, these particular peroxy radicals

685 play no role during daytime and do not contribute to photochemical ozone production.

Net ozone production has a distinct diurnal profile that peaks in the morning (Fig. 5). The peak value of $17\,ppbv\,h^{-1}$ (median) derived only from measurements is higher than that calculated in the model ($11\,ppbv\,h^{-1}$) and shifted to earlier times (Fig. 5). The variability of this peak value is much larger than seen in the model with values up to several ten $ppbv\,h^{-1}$. Differences in the net ozone

690 production derived from the model or radical measurements stem mainly from the underestimation of modelled RO_2 radical concentrations in the morning.

Cl radical may have been an additional source of RO_2. From model sensitivity tests in Section 3.6 with maximum $ClNO_2$ concentration of $0.5\,ppbv$, an integral ozone production rate of about $2\,ppbv$ is calculated during daytime (06:00–18:00). This additional ozone production is small compared to

695   the discrepancy of 20 ppbv between the accumulated modelled ozone production and calculations from radical measurements. Although the Cl initiated RO_2 could have different impacts on the ozone generation than assumed in the model, the additional ozone production from chlorine initiated reactions is most likely not sufficiently large to explain the difference to calculations using measured peroxy radical concentrations.

700   If the discrepancy between measured and modelled k_{OH} is reduced, the modelled ozone production rate better agrees in the morning. This is seen in a model sensitivity run, for which VOC concentrations are scaled to match observed OH reactivity. Modelled RO_2 concentrations increase before 09:00 in this case, but only enhance the daily integral ozone production by 3 ppbv.

During the first period of the campaign (8 June to 14 June) daily maximum ozone mixing ratios
705   increased from 50 to 150 ppbv (Fig. 3). However, the connection between the photochemical ozone production rate and ozone concentrations measured over several days at a distinct location is complicated. Additional ozone loss processes need to be taken into account, for example deposition and indirect loss via reactive nitrogen chemistry during the night (NO_3 and N_2O_5) that are not included in Eq. 5 and 6. Furthermore, the effect of high ozone production in the morning on midday ozone
710   mixing ratios is reduced due to the dilution by the rise of the boundary layer height. Also regional transportation of ozone can be of importance, if the distribution of ozone production and/or loss processes is inhomogeneous. The cumulative ozone production observed during the first period of the campaign is approximately 700 ppbv. This high total ozone production indicates that most of the locally produced ozone could be transported to downwind regions.

715   Previous studies have also found that models underpredict the ozone production rate. Calculations from HO_2 radical measurements resulted in higher ozone production rates (up to a factor of ten) in the early morning at NO concentrations higher than a few ppbv in campaigns in urban and forested environments (Martinez et al., 2003; Ren et al., 2003; Mao et al., 2010; Ren et al., 2013). The high HO_2 in previous campaigns may be partly explained by RO_2 that caused unrecognized interferences
720   in HO_x detection (Fuchs et al., 2011). The shape of the diurnal profile with the high unexplained ozone production rate in the morning, however, is not expected to change much, if also RO_2 is taken into account (Ren et al., 2013), because a good correlation between HO_2 and RO_2 is expected for conditions of high NO concentrations. This was also confirmed by the direct measurement of the total photochemical ozone production rate in one of the studies (Cazorla et al., 2012).

725   **3.9   Budget analysis based on model results**

The budget analysis for OH, HO_2 and RO_2 radicals is based on the results of model calculations. There are two classes of radical reactions. On the one hand, RO_x radicals are produced or destroyed by reactions, in which RO_x radical species are not reactants and products at the same time. On the other hand, RO_x species are converted into each other by radical recycling reactions. In polluted
730   air, during daytime, the conversion reactions are fast, so that the RO_X species are in an equilibrium.

Under these conditions, the impact of primary production and destruction is similar on all radical species regardless which radical species is formed. The partitioning of RO_X, however, depends on the relative rates of the conversion reactions.

3.9.1 Primary radical production and destruction

735 Mean diurnal profiles of primary radical production and destruction rates of RO_x radicals are shown in Fig. 10. Highest turnover rates occur after noontime reaching maximum values around $5\,\mathrm{ppbv\,h^{-1}}$. HONO, O_3 and HCHO photolysis account for approximately two third of the daytime radical production. HONO, O_3 and HCHO as well as their photolysis frequencies are well constrained by measurements. HONO photolysis alone is the most important single primary source with maximum

740 values of nearly $2\,\mathrm{ppbv\,h^{-1}}$ at 13:00. O_3 photolysis contributes $15\,\%$ to the total radical production rate. Formaldehyde photolysis is a major source for HO_2 accounting for $18\,\%$ of total daytime primary production.

Other production processes of OH includes alkene ozonolysis, which also produces HO_2 and RO_2. The remaining part of the daytime production can be attributed to the photolysis of carbonyl

745 compounds.

Recent findings in the understanding of the oxidation of isoprene found that photo-labile hydroxperoxy aldehydes (HPALD) can be formed in environments where radical recycling via NO is not efficient (Peeters et al., 2014). HPALD photolysis can be a significant radical source in this case. In this campaign, this reaction is almost negligible (Fig. 10), because modelled HPALD concentrations

750 are only around $100\,\mathrm{pptv}$.

In the morning (till 10:00), the major loss of RO_x is the reaction of OH with NO_2. At later times, radical destruction is dominated by the loss via peroxy radical self-reactions, HO_2+HO_2, HO_2+RO_2 and RO_2+RO_2. HO_2 and RO_2 concentration values and their diurnal profiles are similar. Because the reaction of HO_2 with RO_2 have the largest reaction rate constant of the three types of peroxy

755 radical self-reactions, these reactions make the largest contribution. The effect of radical destruction by RO_2 self-reactions could be underestimated in the model, because only reactions of RO_2 with methyl-peroxy radicals and acetyl peroxy radicals are included in the RACM mechanism.

The reaction of OH with NO is the only known gas phase production of HONO, which can compensate the OH production by HONO photolysis. During this campaign, however, HONO for-

760 mation in the gas phase is always much smaller compared to HONO photolysis making HONO a net source of OH. This also means that the high HONO concentrations during the day cannot be explained by production from the reaction of OH with NO. The observation of an unusual high HONO concentration of $2\,\mathrm{ppbv}$ at noon of 28 June (Fig. 3), when the nearby agricultural field was treated with artificial nitrogen fertilizer, suggests that HONO emissions from surrounding farmland

765 may have played an important role at the measurement site in Wangdu. An imbalance of the two gas-phase reactions of HONO has also been found in many other field campaigns, for example in

previous field campaigns in China in 2006 (Li et al., 2012). Heterogeneous formation of HONO is thought to explain part of the missing daytime source (VandenBoer et al., 2014, and ref. therein), but also unaccounted gas-phase sources might be of importance (Li et al., 2014).

770   Further radical terminating OH losses include reactions of OH with hydrocarbons that do not lead to radical propagating peroxy radicals.

Compared to our previous campaign in Yufa in 2006, the primary radical production in this campaign is significantly less in the morning mainly because of smaller OH production from HONO photolysis. In the afternoon, however, radical production was mainly due to ozone and formaldehyde

775   photolysis in Yufa. The relative contributions of radical destruction processes are similar in this campaign compared to Yufa, but radical loss due to reactions with nitrogen oxides is less important in the morning and slightly enhanced in the afternoon in this campaign.

3.9.2 Radical propagation reactions

Figure 11 shows the distribution of turnover rates of radical recycling reactions. These conversion

780   reactions establish the partitioning of total RO_x species into OH, HO_2 and RO_2.

The conversion of OH to HO_2 (43 % of the total OH destruction rate) is dominated by the reaction of OH with CO and HCHO contributing 25 % and 13 % to the total OH destruction during daytime. Isoprene and its oxidation products (MVK and MACR) are the dominant organic OH reactants in the afternoon. In contrast, alkenes and aldehydes reactions with OH dominate the conversion from

785   OH to RO_2 in the morning.

The radical recycling from RO_2 to HO_2 and also from HO_2 to OH is mainly driven by NO reactions. NO reactions with methyl peroxy radicals (MO_2) and isoprene derived radicals (ISOP) account for 26 % of the total conversion rate of RO_2 to HO_2 during daytime. Alkane (ALKAP) and alkene (ALKEP) derived peroxy radicals contribute another 20 % and 13 %, respectively. Their

790   relative importance is largest in the morning.

Acyl peroxy radicals (ACO_3 and RCO_3) do not directly convert to HO_2, but form other RO_2 species (MO_2 and ETHP in RACM). A second reaction step with NO is required to form HO_2. Therefore, they are not included in the budget in Fig. 11. However, this conversion reaction contributes to ozone production discussed above. The daytime average turnover rate of this type of

795   conversion reaction is $0.9\,\mathrm{ppbv\,h^{-1}}$.

Direct conversion of RO_2 radicals to HO_2 and OH by isomerization reactions with subsequent decomposition has been found to be competitive with radical recycling via reactions with NO in the isoprene oxidation mechanism (Peeters et al., 2014; Crounse et al., 2012). The effective isomerization rate of isoprene derived RO_2 is $0.01\,\mathrm{s^{-1}}$ for conditions of this campaign in the afternoon

800   hours (temperature: 303 K). This loss rate is small compared to the loss of isoprene derived RO_2 via the reaction with NO. The average NO mixing ratio is $0.19\,\mathrm{ppbv}$ (for the subset of days shown in Fig. 11) giving a loss rate of $0.04\,\mathrm{s^{-1}}$. Therefore, only 20 % of RO_2 from isoprene (ISOP) un-

dergoes isomerization, so that radical recycling from ISOP to HO_2 via isomerization is small. This also explains, why HPALD photolysis as primary RO_x source is not important in this campaign. In contrast to RO_2 from isoprene, one RO_2 species from MACR (MACP) nearly exclusively isomerizes for afternoon conditions of the campaign. However, the overall impact of this radical recycling reaction is also small, because the median production rate of MACP is only $0.14\,\mathrm{ppbv\,h^{-1}}$ in the afternoon.

The maximum turnover rate of recycling reactions is slightly shifted to earlier times compared to the maximum turnover rate of primary radical production. This is mainly due to the dominance of conversion reactions of RO_2 and HO_2 with NO. This can be best seen in the mean diurnal profile of the HO_2 conversion to OH, which peaks earlier than the OH conversion to HO_2 and RO_2 (Fig. 11, lower panel). Because the total OH production and destruction rates equal in the model calculation, this imbalance is compensated by the larger primary OH production (Fig. 10).

Compared to the turnover rates in Yufa 2006, radical conversion is less strong in the morning in this campaign, mainly due to smaller peak NO concentrations leading to a reduced reformation of OH from HO_2. This is accompanied by lower HO_2 production in the reaction of OH with formaldehyde. In the afternoon, the strength of radical conversion reaction is similar in both campaigns.

4 Summary and conclusions

A comprehensive set of measurements was collected to characterize the photochemistry at the rural site Wangdu in the North China Plain in 2014. Air pollution was likely transported from surrounding industrial areas and farmland in the North China Plain and few days were influenced by clean air coming from the North.

OH, HO_2 and RO_2 radicals were measured by a new instrument applying laser induced fluorescence technique. In contrast to most previous studies, RO_2 and HO_2 were measured separately, and HO_2 could be determined without interferences from RO_2. In order to test if OH measurements included artifacts from OH production inside the measurement cell, chemical modulation tests were performed. These tests identified unexplained OH signals equivalent to 0.5 to $1 \times 10^6\,\mathrm{cm^{-3}}$ with a systematic experimental $1\,\sigma$ uncertainty of $0.5 \times 10^6\,\mathrm{cm^{-3}}$. Given this uncertainty, the unexplained OH signal may have been caused by an experimental bias of the chemical modulation setup, but also an unknown OH interference cannot be excluded. In case of an interference, it would have contributed about 10 % of the maximum daytime OH concentration, so that it would have a minor impact on the interpretation of daytime OH measurements. However, it cannot be excluded that nighttime OH measurements were significantly affected by interferences. An improved set-up of this system will be used in future field campaigns.

Daily maximum concentrations of OH, HO_2 and RO_2 ranged from 5 to $15 \times 10^6\,\mathrm{cm^{-3}}$, 3 to $14 \times 10^8\,\mathrm{cm^{-3}}$ and 3 to $15 \times 10^8\,\mathrm{cm^{-3}}$, respectively. Model calculations applying the chemical mech-

anism RACM reproduce the measured radical concentrations generally well in this campaign. The RACM is extended by recent findings in the isoprene chemistry (Peeters et al., 2014; Crounse et al., 2012), but radical concentrations are only slightly enhanced by the additional radical recycling in this campaign.

Like in other field campaigns, measured OH concentrations are larger than model predictions at NO mixing ratios below 0.3 ppbv in the afternoon (Rohrer et al., 2014). However, the measure-to-model ratio is only 1.4 to 2.0 and therefore smaller than in previous campaigns in the Pearl River Delta and North China Plain. In these campaigns, model-measurements ratios were up to a factor 4.5 (Lu et al., 2012, 2013). Like in previous campaigns, introduction of an additional radical recycling process that has the same effect as NO can close the gap between modelled and measured OH. In this campaign, an equivalent of 100 pptv NO would be needed.

Measured RO_2 concentrations are significantly larger than the model predicts in the morning. At the same time measured OH reactivity is smaller than modelled OH reactivity, which suggests missing RO_2 production from unmeasured OH reactants in the model.

To our knowledge, there are not many published studies where measured RO_2 data were available in addition to measured HO_2 (Mihelcic et al., 2003; Ren et al., 2005). Therefore, this study provides the opportunity to calculate the total net ozone production rate from measurements of all peroxy radicals including HO_2 and RO_2. Local net ozone production can then be compared to model results. In the afternoon, both rates agree well, but the model underpredicts the ozone production rate by about $6\,\mathrm{ppbv\,h^{-1}}$ in the morning. This underestimation is caused by underpredicted RO_2 in the model, whereas the modelled HO_2 concentrations agree well with measurements. This result is different from the findings in other studies in urban and forested environments, where the ozone production rate was also underestimated, but caused by too low values of the modelled HO_2 (Martinez et al., 2003; Ren et al., 2003; Mao et al., 2010; Ren et al., 2013).

Radicals are primarily produced by photolysis reactions and radical loss is dominated by reactions with nitrogen oxides in the morning and peroxy radical self-reactions in the afternoon. This is similar to our previous campaign 2006 in Yufa that is also located in the North China Plain (Lu et al., 2013). OH production from HONO photolysis in the afternoon was the largest primary radical source in this campaign. Because NO concentrations are lower than in 2006 in the morning, radical conversion rates are smaller. Higher OH concentrations and OH reactivity measured in 2006 and smaller OH recycling from the reaction of HO_2 with NO in the afternoon led to the need of a larger enhancement of the radical recycling efficiency for the campaign in 2006 compared to results from this campaign.

Acknowledgements. We thank the science teams of Wangdu-2014 Campaign. This work was supported by the National Natural Science Foundation of China (Major Program: 21190052 and Innovative Research Group: 41121004), the Strategic Priority Research Program of the Chinese Academy of Sciences (grant no. XDB05010500), the Collaborative Innovation Center for Regional Environmental Quality, the EU-project AMIS (Fate and Im-

pact of Atmospheric Pollutants, PIRSES-GA-2011-295132). The authors gratefully acknowledge the NOAA

875   Air Resources Laboratory (ARL) for the provision of the HYSPLIT transport and dispersion model and/or

READY website (http://www.ready.noaa.gov) used in this publication.

References

Berresheim, H., Plass-Dülmer, C., Elste, T., Mihalopoulos, N., and Rohrer, F.: OH in the coastal boundary layer of Crete during MINOS: measurements and relationship with ozone photolysis, Atmos. Chem. Phys., 3, 639–649, doi:10.5194/acp-03-639-2003, 2003.

Bohn, B., Corlett, G. K., Gillmann, M., Sanghavi, S., Stange, G., Tensing, E., Vrekoussis, M., Bloss, W. J., Clapp, L. J., Kortner, M., Dorn, H.-P., Monks, P. S., Platt, U., Plass-Dülmer, C., Mihalopoulos, N., Heard, D. E., Clemitshaw, K. C., Meixner, F. X., Prevot, A. S. H., and Schmitt, R.: Photolysis frequency measurement techniques: results of a comparison within the ACCENT project, Atmos. Chem. Phys., 8, 5373–5391, doi:10.5194/acp-08-5373-2008, 2008.

Brauers, T., Hausmann, M., Bister, A., Kraus, A., and Dorn, H.-P.: OH radicals in the boundary layer of the Atlantic Ocean 1. Measurements by long-path laser absorption spectroscopy, J. Geophys. Res., 106, 7399–7414, doi:10.1029/2000jd900679, 2001.

Brown, S. S., and Stutz, J.: Nighttime radical observations and chemistry, Chem. Soc. Rev., 41, 6405–6447, doi:10.1039/c2cs35181a, 2012.

Cazorla, M., Brune, W. H., Ren, X., and Lefer, B.: Direct measurement of ozone production rates in Houston in 2009 and comparison with two estimation methods, Atmos. Chem. Phys., 12, 1203–1212, doi:10.5194/acp-12-1203-2012, 2012.

Crounse, J. D., Paulot, F., Kjaergaard, H. G., and Wennberg, P. O.: Peroxy radical isomerization in the oxidation of isoprene, Phys. Chem. Chem. Phys., 13, 13 607–13 613, doi:10.1039/C1CP21330J, 2011.

Crounse, J. D., Knap, H. C., Ornso, K. B., Jorgensen, S., Paulot, F., Kjaergaard, H. G., and Wennberg, P. O.: On the atmospheric fate of methacrolein: 1. Peroxy radical isomerization following addition of OH and O_2, J. Phys. Chem. A, 116, 5756–5762, doi:10.1021/jp211560u, 2012.

Dong, H. B., Zeng, L. M., Hu, M., Wu, Y. S., Zhang, Y. H., Slanina, J., Zheng, M., Wang, Z. F., and Jansen, R.: Technical Note: The application of an improved gas and aerosol collector for ambient air pollutants in China, Atmos. Chem. Phys., 12, 10 519–10 533, doi:10.5194/acp-12-10519-2012, 2012.

Ehhalt, D. H.: Photooxidation of trace gases in the troposphere, Phys. Chem. Chem. Phys., 1, 5401–5408, doi:10.1039/a905097c, 1999.

Ehhalt, D. H. and Rohrer, F.: Dependence of the OH concentration on solar UV, J. Geophys. Res., 105, 3565–3571, doi:10.1029/1999JD901070, 2000.

Fuchs, H., Hofzumahaus, A., and Holland, F.: Measurement of tropospheric RO_2 and HO_2 radicals by a laser-induced fluorescence instrument, Rev. Sci. Instrum., 79, 084 104, doi:10.1063/1.2968712, 2008.

Fuchs, H., Bohn, B., Hofzumahaus, A., Holland, F., Lu, K. D., Nehr, S., Rohrer, F., and Wahner, A.: Detection of HO_2 by laser-induced fluorescence: calibration and interferences from RO_2 radicals, Atmos. Meas. Tech., 4, 1209–1255, doi:10.5194/amt-4-1209-2011, 2011.

Fuchs, H., Hofzumahaus, A., Rohrer, F., Bohn, B., Brauers, T., Dorn, H.-P., Häseler, R., Holland, F., Kaminski, M., Li, X., Lu, K., Nehr, S., Tillmann, R., Wegener, R., and Wahner, A.: Experimental evidence for efficient hydroxyl radical regeneration in isoprene oxidation, Nature Geosci., 6, 1023–1026, doi:10.1038/NGEO1964, 2013.

Fuchs, H., Acir, I. H., Bohn, B., Brauers, T., Dorn, H. P., Häseler, R., Hofzumahaus, A., Holland, F., Kaminski, M., Li, X., Lu, K., Lutz, A., Nehr, S., Rohrer, F., Tillmann, R., Wegener, R., and Wahner, A.: OH regeneration

from methacrolein oxidation investigated in the atmosphere simulation chamber SAPHIR, Atmos. Chem. Phys., 14, 7895–7908, doi:10.5194/acp-14-7895-2014, 2014.

Fuchs, H., Tan, Z., Hofzumahaus, A., Broch, S., Dorn, H. P., Holland, F., Künstler, C., Gomm, S., Rohrer, F., Schrade, S., Tillmann, R. and Wahner, A., : Investigation of potential interferences in the detection of atmospheric ROx radicals by laser-induced fluorescence under dark conditions, Atmos. Meas. Tech., 9, 1431-1447, doi:10.5194/amt-9-1431-2016, 2016.

Galloway, M. M., Huisman, A. J., Yee, L. D., Chan, A. W. H., Loza, C. L., Seinfeld, J. H., and Keutsch, F. N.: Yields of oxidized volatile organic compounds during the OH radical initiated oxidation of isoprene, methyl vinyl ketone, and methacrolein under high-NO$_x$ conditions, Atmos. Chem. Phys., 11, 10779–10790, doi:10.5194/acp-11-10779-2011, 2011.

Goliff, W. S., Stockwell, W. R., and Lawson, C. V.: The regional atmospheric chemistry mechanism, version 2, Atmos. Environ., 68, 174–185, doi:10.1016/j.atmosenv.2012.11.038, 2013.

Hard, T. M., George, L. A., and O'Brian, R. J.: FAGE determination of tropospheric OH and HO$_2$, J. Atmos. Sci., 52, 3354–3372, 1995.

Heard, D. E. and Pilling, M. J.: Measurement of OH and HO$_2$ in the troposphere, Chem. Rev., 103, 5163-5198, doi:10.1021/cr020522s, 2003.

Hofzumahaus, A., Aschmutat, U., Heßling, M., Holland, F., and Ehhalt, D. H.: The measurement of tropospheric OH radicals by laser-induced fluorescence spectroscopy during POPCORN field campaign, Geophys. Res. Lett., 23, 2541–2544, doi:10.1029/96GL02205, 1996.

Hofzumahaus, A., Rohrer, F., Lu, K., Bohn, B., Brauers, T., Chang, C.-C., Fuchs, H., Holland, F., Kita, K., Kondo, Y., Li, X., Lou, S., Shao, M., Zeng, L., Wahner, A., and Zhang, Y.: Amplified trace gas removal in the troposphere, Science, 324, 1702–1704, doi:10.1126/science.1164566, 2009.

Holland, F., Heßling, M., and Hofzumahaus, A.: In situ measurement of tropospheric OH radicals by laser-induced fluorescence - a description of the KFA instrument, J. Atmos. Sci., 52, 3393–3401, doi:10.1175/1520-0469(1995)052<3393:ISMOTO>2.0.CO;2, 1995.

Holland, F., Hofzumahaus, A., Schäfer, J., Kraus, A., and Pätz, H. W.: Measurements of OH and HO$_2$ radical concentrations and photolysis frequencies during BERLIOZ, J. Geophys. Res., 108, 8246, doi:10.1029/2001JD001393, 2003.

Hua, W., Chen, Z. M., Jie, C. Y., Kondo, Y., Hofzumahaus, A., Takegawa, N., Chang, C. C., Lu, K. D., Miyazaki, Y., Kita, K., Wang, H. L., Zhang, Y. H., and Hu, M.: Atmospheric hydrogen peroxide and organic hydroperoxides during PRIDE-PRD'06, China: their concentration, formation mechanism and contribution to secondary aerosols, Atmos. Chem. Phys., 8, 6755–6773, doi:10.5194/acp-8-6755-2008, 2008.

Kleffmann, J., Gavriloaiei, T., Hofzumahaus, A., Holland, F., Koppmann, R., Rupp, L., Schlosser, E., Siese, M., and Wahner, A.: Daytime formation of nitrous acid: A major source of OH radicals in a forest, Geophys. Res. Lett., 32, L05 818, doi:10.1029/2005GL022524, 2005.

Lelieveld, J., Butler, T. M., Crowley, J. N., Dillon, T. J., Fischer, H., Ganzeveld, L., Harder, H., Lawrence, M. G., Martinez, M., Taraborrelli, D., and Williams, J.: Atmospheric oxidation capacity sustained by a tropical forest, Nature, 452, 737–740, doi:10.1038/nature06870, 2008.

Li, X., Brauers, T., Häseler, R., Bohn, B., Fuchs, H., Hofzumahaus, A., Holland, F., Lou, S., Lu, K. D., Rohrer, F., Hu, M., Zeng, L. M., Zhang, Y. H., Garland, R. M., Su, H., Nowak, A., Wiedensohler, A., Takegawa, N.,

Shao, M., and Wahner, A.: Exploring the atmospheric chemistry of nitrous acid (HONO) at a rural site in Southern China, Atmos. Chem. Phys., 12, 1497–1513, doi:10.5194/acp-12-1497-2012, 2012.

Li, X., Rohrer, F., Hofzumahaus, A., Brauers, T., Hšeler, R., Bohn, B., Broch, S., Fuchs, H., Gomm, S., Holland, F., Jäger, J., Kaiser, J., Keutsch, F. N., Lohse, I., Lu, K., Tillmann, R., Wegener, R., Wolfe, G. M., Mentel, T. F., Kiendler-Scharr, A., and Wahner, A.: Missing gas-phase source of HONO inferred from Zeppelin measurements in the troposphere, Science, 344, 292–296, doi:10.1126/science.1248999, 2014.

Liu, Y., Lu, K., Dong, H., Li, X., Cheng, P., Zou, Q., Wu, Y., Liu, X., and Zhang, Y.: In situ monitoring of atmospheric nitrous acid based on multi-pumping flow system and liquid waveguide capillary cell, Journal of Environmental Sciences-China, 43, 273-284, doi:10.1016/j.jes.2015.11.034, 2016.

Lou, S., Holland, F., Rohrer, F., Lu, K., Bohn, B., Brauers, T., Chang, C. C., Fuchs, H., Häseler, R., Kita, K., Kondo, Y., Li, X., Shao, M., Zeng, L., Wahner, A., Zhang, Y., Wang, W., and Hofzumahaus, A.: Atmospheric OH reactivities in the Pearl River Delta - China in summer 2006: measurement and model results, Atmos. Chem. Phys., 10, 11 243–11 260, doi:10.5194/acp-10-11243-2010, 2010.

Lu, K. D., Zhang, Y., Su, H., Brauers, T., Chou, C. C., Hofzumahaus, A., Liu, S. C., Kita, K., Kondo, Y., Shao, Wahner, A., Wang, J., Wang, X., and Zhu, T.: Oxidant (O_3 + NO_2) production processes and formation regimes in Beijing, J. Geophys. Res., 1115, D7303, doi:10.1029/2009JD012714, 2010.

Lu, K. D., Rohrer, F., Holland, F., Fuchs, H., Bohn, B., Brauers, T., Chang, C. C., Häseler, R., Hu, M., Kita, K., Kondo, Y., Li, X., Lou, S. R., Nehr, S., Shao, M., Zeng, L. M., Wahner, A., Zhang, Y. H., and Hofzumahaus, A.: Observation and modelling of OH and HO_2 concentrations in the Pearl River Delta 2006: a missing OH source in a VOC rich atmosphere, Atmos. Chem. Phys., 12, 1541–1569, doi:10.5194/acp-12-1541-2012, 2012.

Lu, K. D., Hofzumahaus, A., Holland, F., Bohn, B., Brauers, T., Fuchs, H., Hu, M., Häseler, R., Kita, K., Kondo, Y., Li, X., Lou, S. R., Oebel, A., Shao, M., Zeng, L. M., Wahner, A., Zhu, T., Zhang, Y. H., and Rohrer, F.: Missing OH source in a suburban environment near Beijing: observed and modelled OH and HO_2 concentrations in summer 2006, Atmos. Chem. Phys., 13, 1057–1080, doi:10.5194/acp-13-1057-2013, 2013.

Lu, K. D., Rohrer, F., Holland, F., Fuchs, H., Brauers, T., Oebel, A., Dlugi, R., Hu, M., Li, X., Lou, S. R., Shao, M., Zhu, T., Wahner, A., Zhang, Y. H., and Hofzumahaus, A.: Nighttime observation and chemistry of HO_X in the Pearl River Delta and Beijing in summer 2006, Atmos. Chem. Phys., 14, 4979–4999, doi:10.5194/acp-14-4979-2014, 2014.

Mao, J., Jacob, D. J., Evans, M. J., Olson, J. R., Ren, X., Brune, W. H., Clair, J. M. S., Crounse, J. D., Spencer, K. M., Beaver, M. R., Wennberg, P. O., Cubison, M. J., Jimenez, J. L., Fried, A., Weibring, P., Walega, J. G., Hall, S. R., Weinheimer, A. J., Cohen, R. C., Chen, G., Crawford, J. H., McNaughton, C., Clarke, A. D., Jaegle, L., Fisher, J. A., Yantosca, R. M., Le Sager, P., and Carouge, C.: Chemistry of hydrogen oxide radicals (HO_X) in the Arctic troposphere in spring, Atmos. Chem. Phys., 10, 5823–5838, doi:10.5194/acp-10-5823-2010, 2010.

Mao, J., Ren, X., Brune, W. H., Van Duin, D. M., Cohen, R. C., Park, J. H., Goldstein, A. H., Paulot, F., Beaver, M. R., Crounse, J. D., Wennberg, P. O., DiGangi, J. P., Henry, S. B., Keutsch, F. N., Park, C., Schade, G. W., Wolfe, G. M., and Thornton, J. A.: Insights into hydroxyl measurements and atmospheric oxidation in a California forest, Atmos. Chem. Phys., 12, 8009–8020, doi:10.5194/acp-12-8009-2012, 2012.

Martinez, M., Harder, H., Kovacs, T. A., Simpas, J. B., Bassis, J., Lesher, R., Brune, W. H., Frost, G. J., Williams, E. J., Stroud, C. A., Jobson, B. T., Roberts, J. M., Hall, S. R., Shetter, R. E., Wert, B., Fried, A., Alicke, B., Stutz, J., Young, V. L., White, A. B., and Zamora, R. J.: OH and HO_2 concentrations, sources, and loss rates during the Southern Oxidants Study in Nashville, Tennessee, summer 1999, J. Geophys. Res., 108, 4617, doi:10.1029/2003JD003551, 2003.

Mauldin III, R. L., Berndth, T., Sipila, M., Paasonen, P., Petaja, T., Kim, S., Kurten, T., Stratmann, F., Kerminen, V. M., and Kulmala, M.: A new atmospherically relevant oxidant of sulphur dioxide, Nature., 488, 193–196, doi:10.1038/nature11278, 2012.

Mihelcic, D., Holland, F., Hofzumahaus, A., Hoppe, L., Konrad, S., Müsgen, P., Pätz, H.-W., Schäfer, H.-J., Schmitz, T., Volz-Thomas, A., Bächmann, K., Schlomski, S., Platt, U., Geyer, A., Alicke, B. and Moortga, G. K.: Peroxy radicals during BERLIOZ at Pabstthum: Measurements, radical budgets and ozone production, J. Geophys. Res., 108, 8254, doi:10.1029/2001JD001014, 2003.

Min, K. E., Washenfelder, R. A., Dube, W. P., Langford, A. O., Edwards, P. M., Zarzana, K. J., Stutz, J., Lu, K., Rohrer, F., Zhang, Y., and Brown, S. S.: A broadband cavity enhanced absorption spectrometer for aircraft measurements of glyoxal, methylglyoxal, nitrous acid, nitrogen dioxide, and water vapor, Atmos. Meas. Tech. Discuss., 8, 11 209–11 254, doi:10.5194/amtd-8-11209-2015, 2015.

Novelli, A., Hens, K., Tatum Ernest, C., Kubistin, D., Regelin, E., Elste, T., Plass-Dülmer, C., Martinez, M., Lelieveld, J., and Harder, H.: Characterisation of an inlet pre-injector laser-induced fluorescence instrument for the measurement of atmospheric hydroxyl radicals, Atmos. Meas. Tech., 7, 3413–3430, doi:10.5194/amt-7-3413-2014, 2014.

Osthoff, H., Roberts, J. M., Ravishankara, A. R., Williams, E. J., Lerner, B. M., Sommariva, R., Bates, T. S., Coffman, D., Quinn, P. K., Dibb, J. E., Stark, H., Burkholder, J. B., Talukdar, R. K., J. Meagher, Fehsenfeld, F. C. and Brown, S. S.: High levels of nitryl chloride in the polluted subtropical marine boundary layer, Nature Geosci., 1, 324–328, doi:10.1038/ngeo177, 2008.

Ou, J., Yuan, Z., Zheng, J., Huang, Z., Shao, M., Li, Z., Huang, X., Guo, H., Louie, P. K. K.: Ambient ozone control in a photochemically active region: Short-term despiking or long-term attainment?, Environ. Sci. Technol., in press, doi:10.1021/acs.est.6b00345, 2016.

Paulot, F., Crounse, J. D., Kjaergaard, H. G., Kurten, A., St. Clair, J. M., Seinfeld, J. H., and Wennberg, P. O.: Unexpected epoxide formation in the gas-phase photooxidation of isoprene, Science, 325, 730–733, doi:10.1126/science.1172910, 2009.

Peeters, J. and Müller, J.-F.: HO_X radical regeneration in isoprene oxidation via peroxy radical isomerisations. II: experimental evidence and global impact, Phys. Chem. Chem. Phys., 12, 14 227–14 235, doi:10.1039/C0CP00811G, 2010.

Peeters, J., Nguyen, T. L., and Vereecken, L.: HO_X radical regeneration in the oxidation of isoprene, Phys. Chem. Chem. Phys., 11, 5935–5939, doi:10.1039/b908511d, 2009.

Peeters, J., Müller, J.-F., Stavrakou, T., and Nguyen, V. S.: Hydroxyl radical recycling in isoprene oxidation driven by hydrogen bonding and hydrogen tunneling: The upgraded LIM1 mechanism, J. Phys. Chem. A, 118, 8625–8643, doi:10.1021/jp5033146, 2014.

1035   Praske, E., Crounse, J. D., Bates, K. H., Kurten, T., Kjaergaard, H. G., and Wennberg, P. O.: Atmospheric fate
of methyl vinyl ketone: Peroxy radical reactions with NO and HO_2, J. Phys. Chem. A, 119, 4562–4572,
doi:10.1021/jp5107058, 2015.

Ren, X., Harder, H., Martinez, M., Lesher, R. L., Oliger, A., Shirley, T., Adams, J., Simpas, J. B., and Brune,
W. H.: HO_X concentrations and OH reactivity observations in New York City during PMTACS-NY2001,
1040   Atmos. Environ., 37, 3627–3637, 2003.

Ren, X. R., Brune, W. H., Cantrell, C. A., Edwards, G. D., Shirley, T., Metcalf, A. R. and Lesher, R. L.: Hydroxyl
and peroxy radical chemistry in a rural area of Central Pennsylvania: Observations and model comparisons,
J. Atmos. Chem., 52, 231-257, doi:10.1007/s10874-005-3651-7, 2005.

Ren, X., van Duin, D., Cazorla, M., Chen, S., Mao, J., Zhang, L., Brune, W. H., Flynn, J. H., Grossberg,
1045   N., Lefer, B. L., Rappenglück, B., Wong, K. W., Tsai, C., Stutz, J., Dibb, J. E., Thomas Jobson, B., Luke,
W. T., and Kelley, P.: Atmospheric oxidation chemistry and ozone production: Results from SHARP 2009 in
Houston, Texas, J. Geophys. Res., 118, 5770–5780, doi:10.1002/jgrd.50342, 2013.

Rohrer, F. and Berresheim, H.: Strong correlation between levels of tropospheric hydroxyl radicals and solar
ultraviolet radiation, Nature, 442, 184–187, doi:10.1038/nature04924, 2006.

1050   Rohrer, F., Lu, K., Hofzumahaus, A., Bohn, B., Brauers, T., Chang, C.-C., Fuchs, H., Häseler, R., Holland, F.,
Hu, M., Kita, K., Kondo, Y., Li, X., Lou, S., Oebel, A., Shao, M., Zeng, L., Zhu, T., Zhang, Y., and Wahner,
A.: Maximum efficiency in the hydroxyl-radical-based self-cleansing of the troposphere, Nature Geosci., 7,
559–563, doi:10.1038/ngeo2199, 2014.

Shao, M., Tang, X. Y., Zhang, Y. H. and Li, W. J.: City clusters in China: air and surface water pollution, Chem.
1055   Soc. Rev., 4, 353-361, doi:10.1890/1540-9295(2006)004[0353:ccicaa]2.0.co;2, 2006.

Stein, A.F., Draxler, R.R, Rolph, G.D., Stunder, B.J.B., Cohen, M.D., and Ngan, F.,: NOAA's HYS-
PLIT atmospheric transport and dispersion modeling system, Bull. Amer. Meteor. Soc., 96, 2059-2077,
doi:http://dx.doi.org/10.1175/BAMS-D-14-00110.1, 2015.

Stone, D., Whalley, L. K., and Heard, D. E.: Tropospheric OH and HO_2 radicals: field measurements and model
1060   comparisons, Front. Ecol. Environ., 41, 6348–6404, doi:10.1039/C2CS35140D, 2012.

Tan, D., Faloona, I., Simpas, J. B., Brune, W., Shepson, P. B., Couch, T. L., Summer, A. L., Carroll, M. A.,
Thornberry, T., Apel, E., Riemer, D., and Stockwell, W.: HO_X budget in a deciduous forest: results from
the PROPHET summer 1998 campaign, J. Geophys. Res., 106, 24 407–24 427, doi:10.1029/2001JD900016,
2001.

1065   Tham, Y. J., Wang, Z., Li, Q., Yun, H., Wang, W., Wang, X., Xue, L., Lu, K., Ma, N., Bohn, B., Li, X.,
Kecorius, S., Gröss, J., Shao, M., Wiedensohler, A., Zhang, Y. and Wang, T.: Significant concentrations of
nitryl chloride sustained in the morning: Investigations of the causes and impacts on ozone production in
a polluted region of northern China, Atmos. Chem. Phys. Discuss., 2016, 1-34, doi:10.5194/acp-2016-439,
2016.

1070   Thornton, J. A., Kercher, J. P., Riedel, T. P., Wagner, N. L., Cozic, J., Holloway, J. S., Dube, W. P., Wolfe, G. M.,
Quinn, P. K., Middlebrook, A. M., Alexander, B., and Brown, S. S.: A large atomic chlorine source inferred
from mid-continental reactive nitrogen chemistry, Nature, 464, 271-274, doi:10.1038/Nature08905, 2010.

VandenBoer, T. C., Markovic, M. Z., Sanders, J. E., Ren, X., Pusede, S. E., Browne, E. C., Cohen, R. C.,
Zhang, L., Thomas, J., Brune, W. H., and Murphy, J. G.: Evidence for a nitrous acid (HONO) reser-

1075   voir at the ground surface in Bakersfield, CA, during CalNex 2010, J. Geophys. Res., 119, 9093–9106,
        doi:10.1002/2013JD020971, 2014.

Wang, B., Shao, M., Roberts, J. M., Yang, G., Yang, F., Hu, M., Zeng, L., Zhang, Y., and Zhang, J.: Ground-
        based on-line measurements of peroxyacetyl nitrate (PAN) and peroxypropionyl nitrate (PPN) in the Pearl
        River Delta, China, Int. J. Environ. Anal. Chem., 90, 548–559, doi:10.1080/03067310903194972, 2010.

1080   Wang, M., Zeng, L., Lu, S., Shao, M., Liu, X., Yu, X., Chen, W., Yuan, B., Zhang, Q., Hu, M., and
        Zhang, Z.: Development and validation of a cryogen-free automatic gas chromatograph system (GC-
        MS/FID) for online measurements of volatile organic compounds, Analytical Methods, 6, 9424–9434,
        doi:10.1039/C4AY01855A, 2014.

Wang, Q., Shao, M., Liu, Y., William, K., Paul, G., Li, X., Liu, Y., and Lu, S.: Impact of biomass burning
1085   on urban air quality estimated by organic tracers: Guangzhou and Beijing as cases, Atmos. Environ., 41,
        8380–8390, doi:10.1016/j.atmosenv.2007.06.048, 2007.

Wang, H. C., Chen, T., and Lu, K. D.: Measurement of NO_3 and N_2O_5 in the Troposphere, Prog. Chem., 27,
        963-976, doi:10.7536/PC141230, 2015.

Whalley, L. K., Edwards, P. M., Furneaux, K. L., Goddard, A., Ingham, T., Evans, M. J., Stone, D., Hopkins,
1090   J. R., Jones, C. E., Karunaharan, A., Lee, J. D., Lewis, A. C., Monks, P. S., Moller, S. J., and Heard, D. E.:
        Quantifying the magnitude of a missing hydroxyl radical source in a tropical rainforest, Atmos. Chem. Phys.,
        11, 7223–7233, doi:10.5194/acp-11-7223-2011, 2011.

Whalley, L. K., Blitz, M. A., Desservettaz, M., Seakins, P. W., and Heard, D. E.: Reporting the sensitivity of
        laser-induced fluorescence instruments used for HO_2 detection to an interference from RO_2 radicals and
1095   introducing a novel approach that enables HO_2 and certain RO_2 types to be selectively measured, Atmos.
        Meas. Tech., 6, 3425–3440, doi:10.5194/amt-6-3425-2013, 2013.

Xue, L. K., Saunders, S. M., Wang, T., Gao, R., Wang, X. F., Zhang, Q. Z., and Wang, W. X.: Development
        of a chlorine chemistry module for the Master Chemical Mechanism, Geosci. Model Dev., 8, 3151-3162,
        doi:10.5194/gmd-8-3151-2015, 2015.

Table 1. Instruments deployed in the campaign and used for data analysis.

Parameters	Measurement technique	Time resolution	Detection limit[a]	Accuracy [b]
OH	LIF [c]	32 s	$0.32 \times 10^6 \, cm^{-3}$	±11 %
HO$_2$	LIF [c][d]	32 s	$0.10 \times 10^8 \, cm^{-3}$	±16 %
RO$_2$	LIF [c][d]	32 s	$0.05 \times 10^8 \, cm^{-3}$	±18 %
k_{OH}	LP-LIF [e]	180 s	$0.3 \, s^{-1}$	±10 % ±0.7 s^{-1}
photolysis frequency	spectroradiometer	20 s	[f]	±10 %
O$_3$	UV photometry	60 s	0.5 ppbv	±5 %
NO	chemiluminescence	180 s	60 pptv	±20 %
NO$_2$	chemiluminescence[g]	60s	300 pptv	±20 %
HONO	LOPAP[h]	30s	7 pptv	±20 %
CO, CH$_4$, CO$_2$, H$_2$O	cavity ring down	60 s	[i]	[j]
SO$_2$	pulsed UV fluorescence	60 s	0.1 ppbv	±5 %
HCHO	Hantzsch fluorimetry	60 s	25 pptv	±5 %
volatile organic compounds[k]	GC-FID/MS [l]	1 h	20 to 300 pptv	±15 to 20 %
volatile organic compounds[m]	PTR-MS	20 s	0.2 ppbv	±15 %

[a] signal to noise ratio = 2

[b] 1 σ accuracy or 1 σ calibration uncertainty

[c] laser induced fluorescence

[d] chemical conversion via NO reaction before detection

[e] laser photolysis - laser induced fluorescence

[f] process specific, 5 order of magnitudes lower than maximum in noon time

[g] photolytical conversion to NO before detection, home built converter

[h] long-path absorption photometry

[i] species specific, for CO: 1 ppbv; CH$_4$:1 ppbv; CO$_2$: 25 ppbv; H$_2$O: 0.1 % (absolute water vapor content);

[j] species specific, for CO: 1 ppbv; CH$_4$:±1 ppbv; CO$_2$: ±25 ppbv; H$_2$O: ±5 %

[k] VOCs including C$_2$-C$_{11}$ alkanes, C$_2$-C$_6$ alkenes, C$_6$-C$_{10}$ aromatics

[l] gas chromatography equipped with mass spectrometer and a flame ionization detector

[m] OVOCs including acetaldehyde, methyl-vinyl ketone and methacrolein

Table 2. Assignment of measured VOCs to species in the RACM.

RACM	Measured hydrocarbons
CH4	methane
ETH	ethane
HC3	propane, i-butane, n-butane, 2,2-dimethybutane
HC5	i-pentane, n-pentane, cyclopentane, n-hexane, 2,3-dimethylbutane, 2-methylpentane, 3-methylpentane, n-heptane, 2,4-dimethylpentane, 2,3-dimethypentane, methylcyclopentane, 2-methylhexane, MTBE
HC8	cyclohexane, 3-methylhexane,2,2,4-trimethylpentane, 2,3,4-trimethylpentane, n-heptane, methylcyclohexane, 2-methylheptane, 3-methylheptane, n-octane, n-nonane, n-decane
ETE	ethene
DIEN	1,3-butadiene
OLI	trans-2-butene, cis-butene, trans-2-pentene, cis-2-pentene
OLT	propene,1-butene, i-butene, 1-pentene, 1-hexene, styrene
ACE	ethyne
ISO	isoprene
BEN	benzene
TOL	toluene, ethylbenzene, i-propylbenzene, n-propylbenzene
XYM	m-ethyltoluene, 1,3,5-trimethylbenzene, 1,2,4-trimethylbenzene, 1,2,3-trimethylbenzene, m-diethylbenzene
XYO	o-xylene, o-ethyltoluene
XYP	m-p-xylene, p-ethyltoluene, p-diethylbenzene
HCHO	formaldehyde
ACD	acetaldehyde
MVK/MACR	methyl vinyl ketone and methacrolein

Table 3. Median values of measured species for morning and afternoon hours.

	06:00–10:00	12:00–16:00
$j(O^1D) / 10^{-5}\,s^{-1}$	0.63	1.3
$j(NO_2) / 10^{-3}\,s^{-1}$	3.5	4.9
$OH / 10^6\,cm^{-3}$	3.8	6.9
$HO_2 / 10^8\,cm^{-3}$	1.9	7.4
$RO_2 / 10^8\,cm^{-3}$	3.2	8.8
k_{OH} / s^{-1}	20	11
NO /ppbv	2.5	0.25
NO_2 /ppbv	12	3.3
HONO /ppbv	0.78	0.51
O_3 /ppbv	39	93
CO /ppmv	0.70	0.54
CH_4 /ppmv	2.2	2.0
ISO / ppbv	0.59	0.84
ETH / ppbv	4.1	2.7
HC3 / ppbv	4.0	2.0
HC5 / ppbv	2.5	1.0
HC8 / ppbv	0.57	0.22
ETE / ppbv	3.3	0.93
OLI / ppbv	0.25	0.20
OLT / ppbv	0.83	0.21
BEN / ppbv	1.3	0.71
TOL / ppbv	1.6	0.69
HCHO / ppbv	8.4	7.5
ACD / ppbv	2.6	1.9
MACR / pbv	0.36	0.28
MVK / ppbv	0.54	0.43

Table 4. Modifications in the isoprene oxidation mechanism applied to the model (RACM).

reaction	reaction rate constant / $cm^3 s^{-1}$	reference
ISOP–>MACR+HCHO+OH	$0.31 \times 1.8 \times 10^{11} \times \exp(-9752/T))$	a
ISOP–>MVK+HCHO+OH	$0.62 \times 1.04 \times 10^{11} \times \exp(-9746/T))$	a
ISOP–> HPALD1+HO2+HPCARPO2	$0.5 \times 0.62 \times (9.5 \times 10^7 \exp(-7009/T) + 1.79 \times 10^{-7} \exp(3722.5/T) \times k_{tr})$	a
ISOP–> HPALD2+HO2+HPCARPO2	$0.5 \times 0.31 \times (3.8 \times 10^{13} \exp(-10745/T) + 5.82 \times 10^{-2} \exp(476.3/T) \times k_{tr})$	a
HPALD1+HV–>OH+HO2+0.5×HKET +0.5×MGLY+0.5×ALD+HCHO	$100 \times$ jmacr	b
HPALD2+HV–>OH+HO2+0.5×HKET +0.5×GLY+0.5×ALD+HCHO	$100 \times$ jmacr	b
HPALD1+OH–>OH	4.6×10^{-11}	b
HPALD2+OH–>OH	4.6×10^{-11}	b
HPCARPO2–>CO+OH+OP2	0.1	a
HPCARPO2+NO–>NO2+MGLY+OH+OP2	$2.9 \times 10^{-12} \exp(-300/T)$	a
HPCARPO2+HO2–> OP2	$7.5 \times 10^{-13} \exp(-700/T)$	a
ISHP+OH–>IEPOX+OH	$1.9 \times 10^{-11} \exp(-390/T)$	c
ISHP+OH–>0.7×ISOP+0.3×MACR+0.3×OH	$0.38 \times 10^{-11} \exp(-200/T)$	c
IEPOX+OH–>IEPOXO2	$5.78 \times 10^{-11} \exp(-400/T)$	c
IEPOXO2+NO–>IEPOXO+NO2	$2.54 \times 10^{-12} \exp(-360/T)$	
IEPOXO2+HO2–>IEPOXO+OH+O2	$0.074 \times 10^{-11} \exp(-700/T)$	c
IEPOXO–>0.125×OH+0.825×HO2+0.251×CO +0.725×HKET+0.275×GLY+0.275×ALD +0.074×ORA1+0.275×MGLY+0.375×HCHO	1×10^6	c
MCP–>HKET+OH+CO	$2.9 \times 10^7 \exp(-5297/T)$	d
MACP+NO–>0.65×MO2+0.65×CO +0.35×ACO3+NO2+HCHO	$2.54 \times 10^{-12} \exp(-360/T)$	d
MCP+NO–>NO2+HO2+HKET+CO	$2.54 \times 10^{-12} \exp(-360/T)$	d
MVKP+HO2–>OP2	$0.34 \times 2.91 \times 10^{-13} \exp(-1300/T)$	e
MVKP+HO2–>ACO3+OH+ALD	$0.48 \times 2.91 \times 10^{-13} \exp(-1300/T)$	e
MVKP+HO2–>HO2+OH+ORA2	$0.18 \times 2.91 \times 10^{-13} \exp(-1300/T)$	e

[a] Peeters et al. (2014)
[b] Peeters and Müller (2010)
[c] Paulot et al. (2009)
[d] Crounse et al. (2012)
[e] Praske et al. (2015)
k_{tr}=(NO$\times 2.43 \times 10^{-12}$ exp(-360./T)+HO2$\times 2.05 \times 10^{-13}$ exp(-1300./T)+ACO3$\times 8.4 \times 10^{-14}$ exp(-221./T)+MO2$\times 3.4 \times 10^{-14}$ exp(-221./T))))
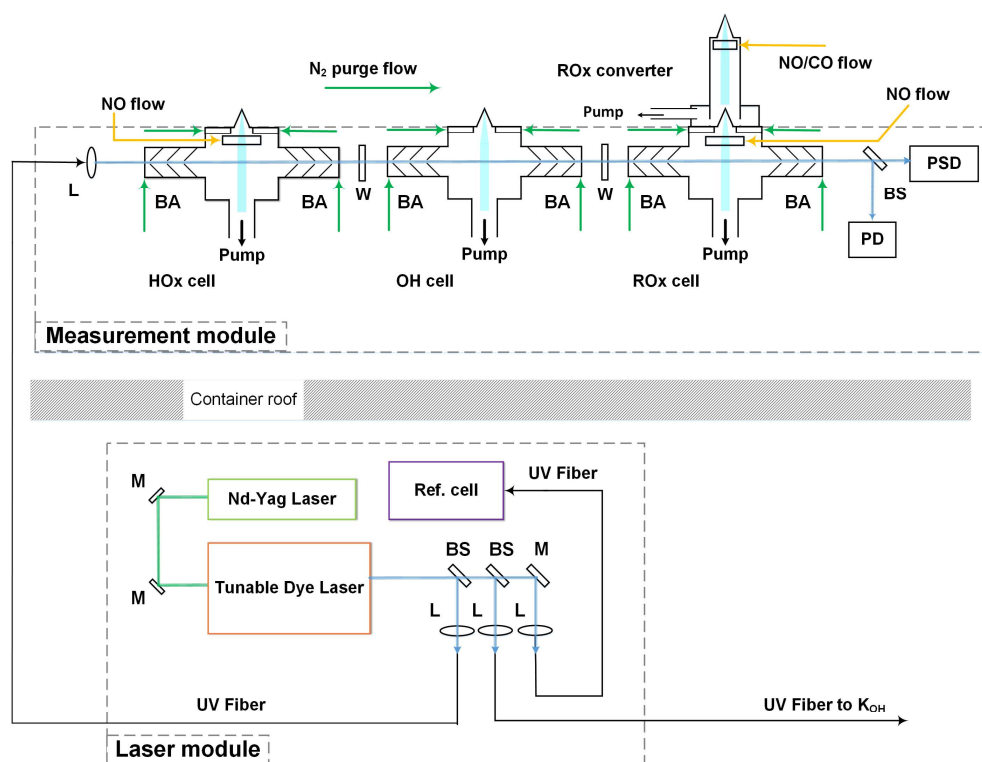
Figure 1. Schematic drawing of the LIF instrument for the detection of OH, HO_2 and RO_2. The laser module and the measurement module were installed inside and on top of a sea container, respectively. 308 nm laserlight is split into three parts (BS: beam splitter, L: lens) and guided by optical fibers to the measurement cells, the k_{OH} instrument and the reference cell. Ambient air is sampled into low pressure fluorescence cells that are separated by windows (W). Reactive gases (NO, CO) are added into the HO_x- and RO_x- cells and the RO_x converter. Baffle arms (BA) and fluorescence cells are continuously purged with N_2. The position and the power of the laser beam are monitored by a photodiode (PD) and a position-sensitive diode (PSD).
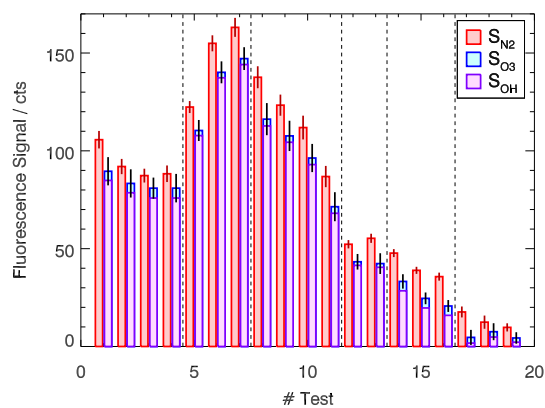
Figure 2. Results of chemical OH modulation tests performed during the campaign. In each test, the total measured OH signal without OH scavenger (S_{N2}, red column) is compared to the sum known contributions from ambient OH (S_{OH}, purple column) and the small, known interference from O_3 (S_{O3}, blue column). A fluorescence signal of 100 cts corresponds to an OH concentration of $6.8 \times 10^6 \, \mathrm{cm}^{-3}$.
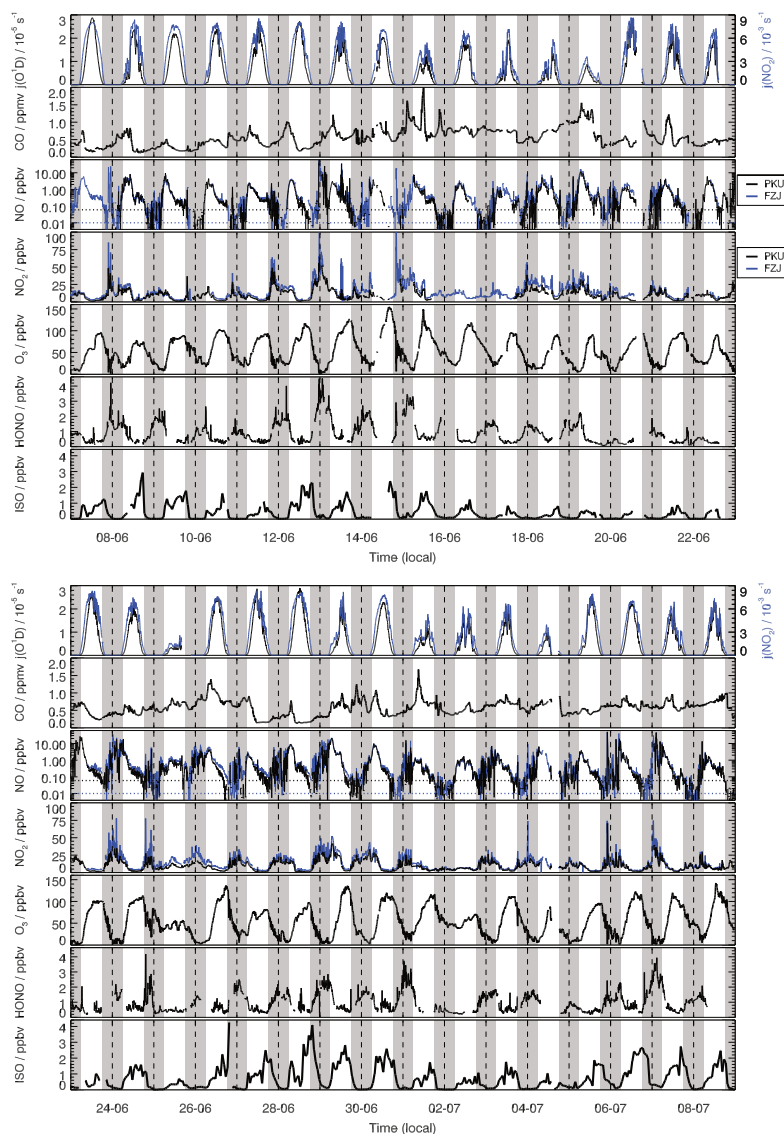
Figure 3. Time series (5-minute data) of measurements during this campaign for j(O^{1}D), j(NO$_2$), CO, NO, NO$_2$, HONO, O$_3$ and isoprene (ISO) used as constraints for model calculations. Vertical, dashed lines denote midnight. Several species were measured by two instruments provided by PKU and FZJ. Measurements of both instruments for O$_3$ and CO well agreed, so that data sets were combined to close data gaps. Only the combined data set is shown here, but different colors indicate the origin of data. NO$_2$ and NO mixing ratios measured by the PKU instruments were generally 20 % smaller than those measured by the FZJ instrument. The horizontal lines denote the limit of detection for two NO instruments (10 pptv for FZJ; 60 pptv for PKU;). Both time series are shown, but measurements from the PKU instruments were used as model constraints.
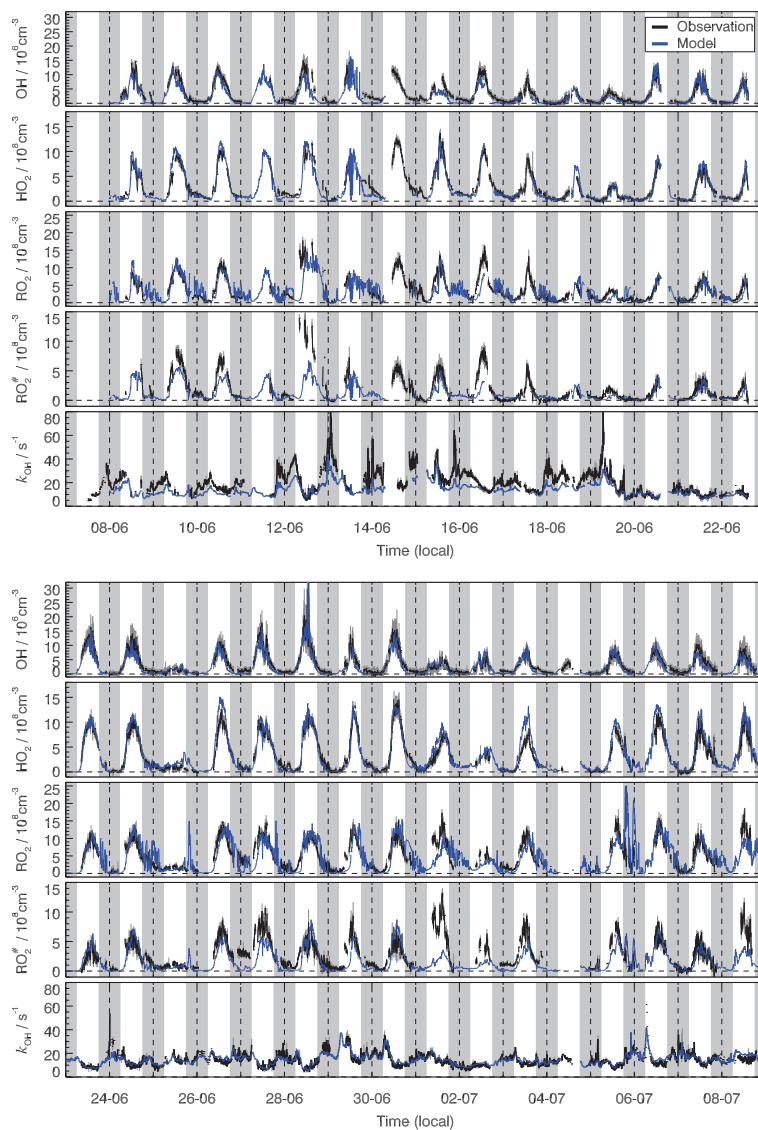
Figure 4. Time series of measured and modelled OH, HO$_2$, RO$_2^{\#}$, total RO$_2$ concentrations and k_{OH}. Vertical, dashed lines denote midnight. See text for details of the definition of RO$_2^{\#}$ and total RO$_2$. Grey vertical lines denote 1 σ standard deviation for measured radicals concentration with respect to 5 min variability.
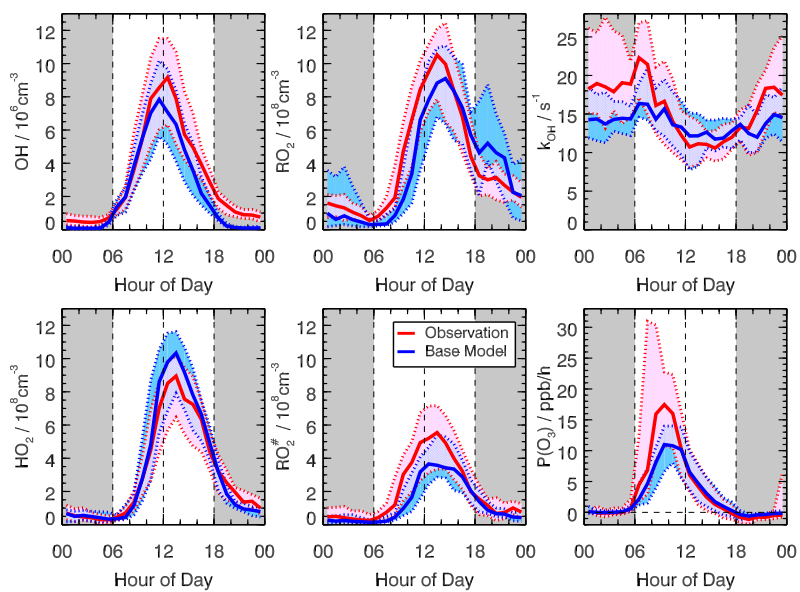
Figure 5. Comparison of hourly median diurnal profiles of OH, HO_2, RO_2, $RO_2^{\#}$ concentrations and k_{OH} and the ozone production rate $P(O_3)$ (thick lines give median values, colored areas give 25 % and 75 % percentiles).
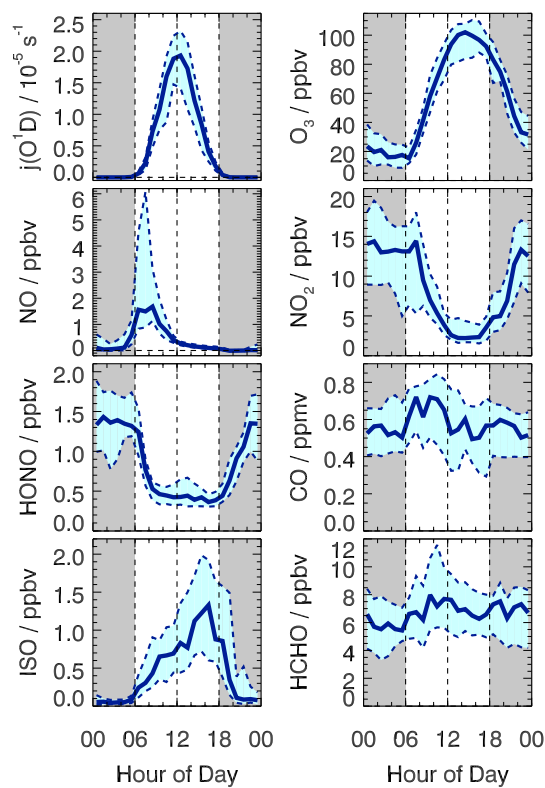
Figure 6. Hourly median diurnal profiles of measured j(O^{1}D), O$_3$, NO, NO$_2$, HONO, CO, isoprene (ISO) and HCHO (thick lines give median values, colored areas give 25 % and 75 % percentiles).
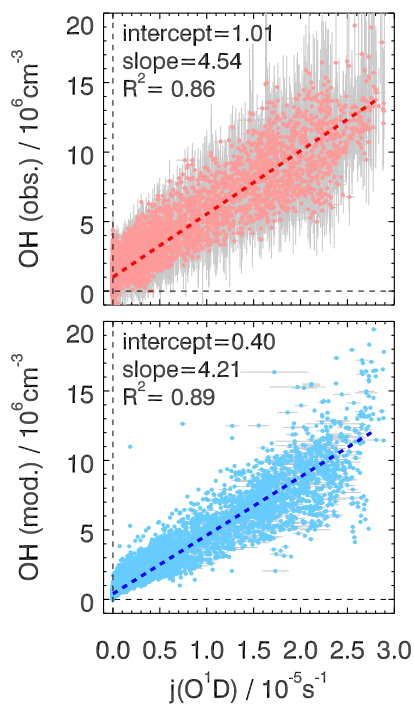
Figure 7. Correlation between $j(O^1D)$ and measured (upper panel) and modelled OH (lower panel). A linear fit is applied, which takes errors in both measurements into account.
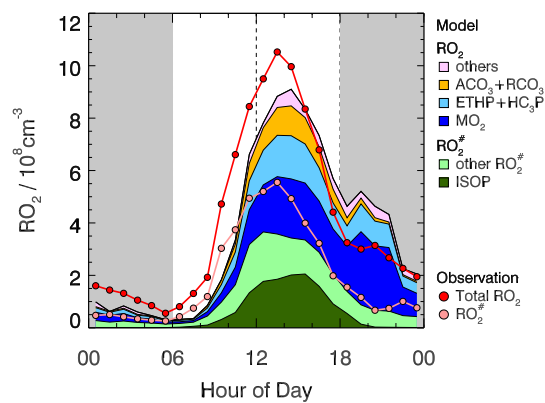
Figure 8. Hourly median diurnal profiles of measured and modelled RO_2 concentrations. Measurements can distinguish between total RO_2 concentrations and the subclass of $RO_2^{\#}$. Modelled RO_2 species are shown as colored areas. Other RO_2 radicals in the evening are mainly RO_2 species produced by the reaction of organic compounds with NO_3.
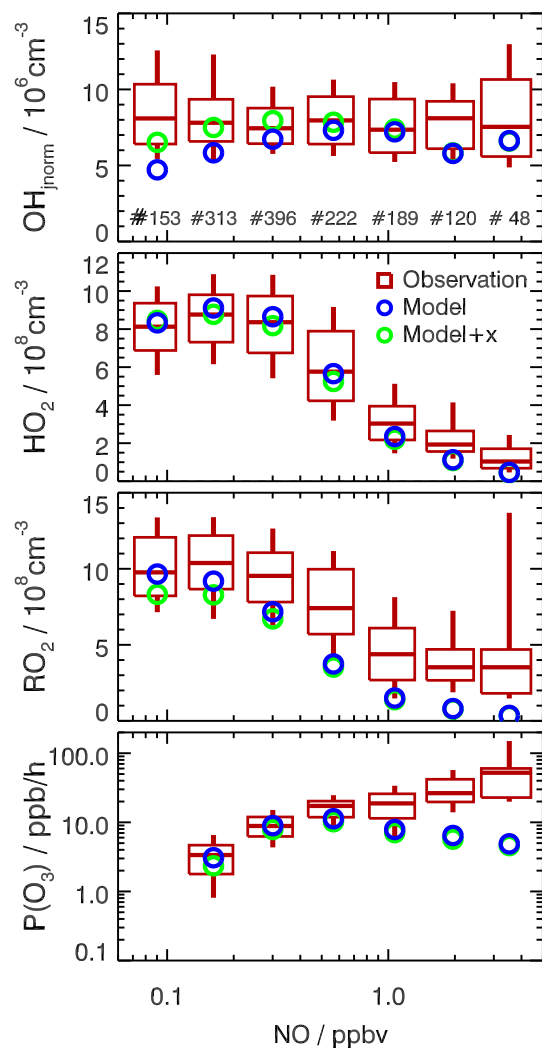
Figure 9. NO dependence of OH, HO$_2$ and RO$_2$ concentrations and instantaneous ozone production rate (P(O$_3$)) for daytime conditions (j(O^{1}D) $> 0.5 \times 10^5$ s^{-1}). OH concentrations are normalized to the average of j(O^{1}D) (1.5×10^{-5} s^{-1}). Boxes give 75 % and 25 % percentiles the center lines the median, and vertical lines 90 % and 10 % percentiles for NO intervals of Δln(NO)/ppbv=0.57. Numbers in the upper panel give the number of data points included in the analysis of each NO interval. Only median values are shown for model results. Results from the base model and with additional radical recycling by a species X (equivalent to 100 pptv NO) are plotted.
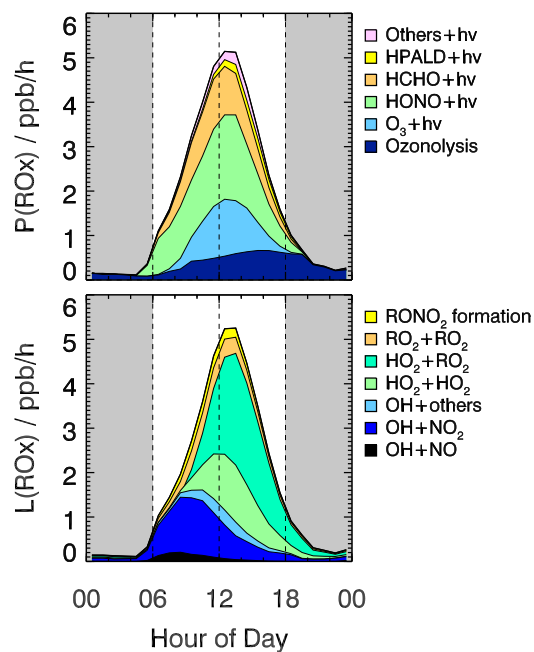
Figure 10. Hourly median diurnal profiles of modelled rates of primary RO_x production and termination reactions.
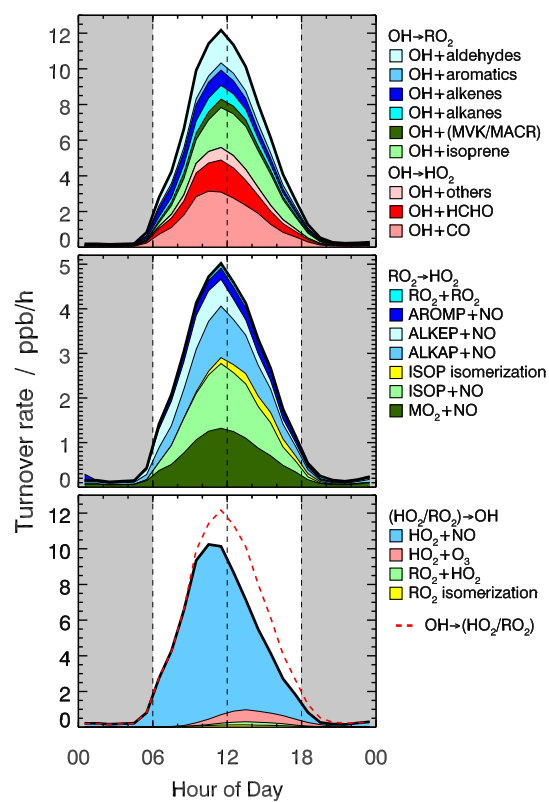
Figure 11. Hourly median diurnal profiles of turnover rates (model results) of radical propagation reactions between OH, HO$_2$ and RO$_2$ radicals.